



Fitzgibbon, T. A., Woodgate, M. A., Barakos, G. N. and Markiewicz, R. H. (2021) Rotor-blade planform design based on an overset harmonic-balance-adjoint optimisation framework. *AIAA Journal*, (doi: 10.2514/1.J060175).

There may be differences between this version and the published version. You are advised to consult the publisher's version if you wish to cite from it.

<http://eprints.gla.ac.uk/243099/>

Deposited on: 2 June 2021

Rotor Blade Planform Design based on an Overset Harmonic Balance Adjoint Optimisation Framework.

T. A. Fitzgibbon*, M. A. Woodgate † G. N. Barakos‡

CFD Laboratory, School of Engineering, University of Glasgow, G12 8QQ Glasgow, UK

R. H. Markiewicz§

DSTL Platform Systems Division, Portsdown West, Portsdown Hill Road, Fareham, Hampshire, PO17 6AD, UK

Optimisation methods in conjunction with CFD are a key tool in advancing current rotor design. High-fidelity optimisation of unsteady rotor flows in forward flight, however, is a challenging problem due to the high computational resources required. To minimize the computational costs, a fully-turbulent, overset, adjoint, harmonic balance, optimisation framework has been developed, which maintains the fidelity of the Navier-Stokes equations. The framework is demonstrated in the aerodynamic re-design of the AH-64A rotor blade. An analysis of the optimised rotor blade is presented, including the key design features that contribute to the performance benefits in each of the examined design conditions. In particular, the benefits and drawbacks of rotor designs with an offloaded blade tip have been discussed. The formulation of the optimisation objective function, blade surface parameterisation and treatment of trim were seen to have an impact on the final planform shape, and have been deemed to be key in obtaining a practical rotor design suitable for use on real-life helicopters.

Nomenclature

a	= speed of sound, m/s
c	= rotor chord, m
C_l	= blade section lift coefficient, $dL/dr \times 2/(\rho c_{ref} (\Omega r)^2)$
C_p	= pressure coefficient, $(p - p_\infty)/(1/2\rho(\Omega r)^2)$
C_q	= blade section torque coefficient, $dQ/dr \times 2/(\rho c_{ref} R (\Omega r)^2)$
C_Q	= torque coefficient (US), $Q/(\rho(\Omega R)^2 \pi R^3)$
C_t	= blade section thrust coefficient, $dT/dr \times 2/(\rho c_{ref} (\Omega r)^2)$
C_T	= thrust coefficient (US), $T/(\rho(\Omega R)^2 \pi R^2)$

*PhD Student, CFD Laboratory, School of Engineering. Email: t.fitzgibbon.1@research.gla.ac.uk

†Research Associate, CFD Laboratory, School of Engineering. Email: mark.woodgate@glasgow.ac.uk

‡Professor, MAIAA, MRAeS, CFD Laboratory, School of Engineering. Email: George.Barakos@glasgow.ac.uk, corresponding author

§Principal Rotorcraft Systems Engineer, Platform Systems Division, DSTL. Email: rhmarkiewicz@mail.dstl.gov.uk

D	= Fourier collocation derivative operator or drag force, N
FoM	= figure of merit, $C_T^{3/2}/(\sqrt{2}C_Q)$
g_j	= design equality constraint functions
h_k	= design inequality constraint functions
I	= design objective function
J	= Jacobian matrix
L	= lift force, N
M	= Mach number, V_∞/a_∞
M_{tip}	= blade tip Mach number, $\mathcal{Q}R/a_\infty$
n	= number of design variables
\mathbf{N}	= mesh metrics vector
N_H	= harmonic balance modes number
m	= number of inequality constraints
p	= number of equality constraints or pressure, Pa
Q	= rotor torque, Nm
R	= rotor radius, m
\mathbf{R}	= flow equation spatial residual vector
\mathbf{R}^*	= flow equation full residual vector
Re	= Reynolds number, $V_{tip}c_{ref}/\nu$
r	= local radial position, m
S	= flow equation source term
t	= time, s
T	= rotor thrust, N
V	= velocity, m/s
\mathbf{V}	= flow equation cell volume vector
\mathbf{W}	= flow equation solution vector
X_s	= surface mesh
X_v	= volume mesh
y	= dimensional wall distance, m
y^+	= dimensionless wall distance, $y\sqrt{\tau_w/\rho}/\nu$
α	= angle of attack, deg
$\boldsymbol{\alpha}$	= design variable vector

α_s	=	shaft angle, deg
β_0	=	coning angle, deg
θ_0	=	collective angle, deg
θ_{1s}, θ_{1c}	=	pitching harmonics, deg
λ	=	adjoint variable vector
μ	=	rotor advance ratio, M_∞/M_{tip}
ν	=	kinematic viscosity, m/s^2
ρ	=	density, kg/m^3
τ_w	=	wall shear stress, Pa
ω	=	reduced frequency
Ω	=	rotor rotational speed, rad/s
hb	=	harmonic balance
ref	=	reference value
tip	=	blade-tip value
i, j, k	=	cell index
∞	=	freestream value

I. Introduction

Rotor design is still an important topic within the rotorcraft community despite the maturity of the baseline helicopter configuration - main rotor/tail rotor. Improved rotor designs can lead to reduced fuel consumption, expanded flight envelopes as well as reduced noise/vibration. The emergence of more advanced planform shapes such as the British Experimental Rotor Programme (BERP) design [1], Blue-Edge blade [2] or Advanced Chinook Rotor Blade (ACRB) [3] show us that rotor design is still progressing. Rotor design practices, however, have significantly changed over the years. In the past, the majority of rotor blades were designed primarily through experimental testing (and preliminary analytical studies). This includes many rotors that still fly today, such as the UH-60A [4], AH-64A [5], S-76 [6], CH-47 [7] or BERP III [8]. However, numerical methods have seen a wider use in rotor design in the past 20-30 years. Boeing developed a new composite blade for the AH-64 helicopter [9] using low and mid-fidelity tools such as CAMRAD [10, 11], EHPIC [12] and LSAF [13]. Here, the designs were primarily evaluated in a parametric manner with limited use of optimisation methods (optimised blade twist in hover and structural mass/stiffness distributions). A more recent rotor design from Boeing includes the ACRB blade [3], however, information as to what design methods were used in this programme are not available in open literature. Another advanced rotor design study included the development of the BERP IV blade [1] as an upgrade to the BERP III design. Here, a combination of wind tunnel testing, preliminary

CFD (**Computational Fluid Dynamics**) studies and mid-fidelity in-house rotor codes were used, without the formal use of optimisation methods. The design of the Blue-Edge blade [2], developed from the ERATO blade, included parametric studies of the planform shape and for the first time optimisation using high-fidelity CFD in hover. Rotor design optimisation studies in industry [14–16], however, are still limited to low/mid-fidelity tools in forward flight. This is primarily due to high computational resources for optimisation of unsteady flows and high turnaround times required in an industrial setting. However, to accurately capture the flow physics around advanced planform shapes, high fidelity Navier-Stokes methods are required.

For these reasons high-fidelity rotor design optimisation has become an important topic of current research within the rotorcraft community, as indicated by recent collaboration programmes [17]. While a considerable number of works can be found on steady-state hover optimisation [18–20], only a few high-fidelity optimisation studies in forward flight exist in literature. The majority of these studies are performed using non-gradient based optimisation methods, which are very expensive in their nature, due to the number of evaluations required being of order $n^2 - n^3$ [21], where n is the number of design parameters. To minimize the computational costs, surrogate modelling based on various techniques such as **kriging** [22], neural networks [23] or latin hypercube sampling (LHS) and radial basis functions (RBF) [24, 25] have been employed. Variable-fidelity surrogate models have also been proven to be successful [26, 27], although highlighted the importance of including high-fidelity simulations in the optimisation framework [26]. These studies, however, either employed a low number of design parameters (under 10) or required a high number of evaluations to form the Design of Experiment (DoE) and update the accuracy of the surrogate model.

Gradient-based methods offer a promising alternative in terms of computational costs. While, they do not guarantee a global optimum, significantly fewer CFD simulations are required to reach a better design. In particular, efficient computation of the design sensitivities can be performed using the adjoint method. The design parameter gradients can be obtained at the cost of a base flow solution irrespective of the number of design variables. The power of the adjoint method has been demonstrated in the fixed-wing community where nearly 1000 variables have been used [28]. The difficulty of rotor optimisation in forward flight, however, is the need for adjoint evaluations of unsteady flow-fields. High-fidelity time-accurate adjoint optimisation frameworks have been developed at NASA [29, 30] and University of Wyoming [31, 32]. These frameworks have included aeroelastic effects through loose/tight-coupling analysis and trim constraints. However, the main drawback of such methods are the high computational costs of time-accurate CFD solutions and the requirement to store the entire time history of the flowfield in memory or **directly on the hard-drive**. This is extremely prohibitive for industrial scale problems, **with improvements relying on algorithmic advancements and exascale computing capabilities**. These issues are a topic of on-going research and include advanced checkpointing techniques [33] or compressing the flow solution time-history through methods such as Proper Orthogonal Decomposition (POD) [34].

To reduce the computational costs associated with unsteady adjoint-based design time-spectral methods have

received particular attention. These methods allow to treat the solution as a large steady problem by assuming periodicity in time, with an additional unsteady source term. The harmonic balance method first gained popularity in the field of turbomachinery [35–37], but has also been applied to rotorcraft problems [38–42]. One-shot harmonic balance methods [43] have also been in development, suitable for fully coupled CFD/CSD (**Computational Structural Dynamics**) analyses and problems with an unknown dominant excitation frequency. While the accuracy and computational costs are directly dependent on the number of modes used in the solution, significant improvements in simulation times are obtainable with only a minor decrease in accuracy when compared to time-marching simulations [42, 44].

The nature of frequency domain methods also make them attractive for adjoint optimisation studies, as the steady adjoint solver (with certain modifications) can be used. The use of harmonic balance-adjoint methods is still an ongoing subject of research as indicated by recent relevant literature. An inviscid harmonic balance adjoint method has been applied in turbomachinery studies (in axial flow) by Huang et al. [45] primarily for two-dimensional simulations. More recently, Rubino [46, 47] developed a fully-turbulent time-spectral adjoint method in SU2, and also applied it only to two-dimensional turbomachinery flows. Following this work, Vitale et al. [48] used the developed method in three-dimensional studies of multi-stage turbomachinery design. Time-spectral adjoint has also been applied in 2D flutter studies [49, 50] and 2D optimisation under periodic wakes [51]. The only application of the time-spectral adjoint to rotorcraft was presented by Choi et al. [52] in a optimisation study of the UH-60A rotor blade. The optimisation, however, was performed for inviscid flows and using a single blade assumption for a coarse matched grid (0.55M nodes). This limits the optimisation framework to flows where viscous effects are not significant and the wake of the other blades does not affect the performance results significantly. Kim et al. [53] extended the framework developed by Choi [52] to include coupled fluid-structure interaction, although no formal optimisation study was shown. The simplifications in current time-spectral adjoint implementations are mainly due to numerical modelling aspects. Including viscous effects leading to higher stiffness of the harmonic balance and adjoint computations. Edgewise rotorcraft flows are also highly complex that include multiple near blade-vortex interactions, leading greater numerical issues including reduced robustness and convergence.

To improve the fidelity of frequency domain adjoint methods found in literature, we have developed a viscous overset harmonic balance adjoint optimisation framework. The use of overset grids improves the grid quality, improving the accuracy and robustness of the solution. The inclusion of viscous effects can lead to different rotor designs, especially when planform is concerned. Finally, we also demonstrate the framework for multiple rotor-blade solutions, and hence, including unsteady wake effects. The developed framework is applied to the re-design of the AH-64A blade for aerodynamic performance improvement in hover and forward flight. We believe this is the first time, a fully-turbulent overset harmonic balance adjoint framework has been applied to rotorcraft flows in forward flight.

The structure of the paper is as follows: first, the coupled adjoint harmonic balance optimisation framework is

presented. Next, validation studies are performed for the AH-64A rotor blade. An optimisation of the AH-64A rotor blade is then performed in hover and forward flight to showcase the capabilities of the developed framework. Finally, the conclusions and future work are presented.

II. Numerical Methods

A. Fully-implicit HMB3 Solver

The multi-block structured Helicopter Multi-Block (HMB3) [54, 55] code is used as the CFD solver for the present work. The Navier-Stokes equations are discretised using a cell-centred finite volume approach on a multi-block grid. The semidiscrete form of the system of ordinary differential equations for the three solution formulations applied within this work are shown in equations 1-3.

$$\frac{d\mathbf{W}}{d\tau} + \mathbf{R}(\mathbf{W}) = \mathbf{S} \quad \text{Steady} \quad (1)$$

$$\frac{d\mathbf{W}}{dt} + \frac{d\mathbf{W}}{d\tau} + \mathbf{R}^*(\mathbf{W}) = 0 \quad \text{Unsteady} \quad (2)$$

$$\frac{d\mathbf{W}_{hb}}{d\tau} + \omega D\mathbf{W}_{hb} + \mathbf{R}_{hb}(\mathbf{W}_{hb}) = 0 \quad \text{HB} \quad (3)$$

where, \mathbf{W} is the vector of conserved variables, \mathbf{R} is the spatial residual vector, \mathbf{R}^* is the full residual vector, \mathbf{S} is the source term, t is the real time step, τ is the pseudo time step, ω is the reduced frequency, D is the Fourier collocation derivative operator and HB refers to the Harmonic Balance method.

For all methods, to evaluate the convective fluxes, Osher's[56] approximate Riemann solver is used, while the viscous terms are discretised using a second order central differencing spatial discretisation. The Monotone Upstream-centred Schemes for Conservation Laws, which is referred to in the literature as the MUSCL approach and developed by van Leer [57], is used to provide formally 3rd order accuracy in space. The HMB3 solver uses the alternative form of the Albada limiter [58] being activated in regions where large gradients are encountered mainly due to shock waves, avoiding the non-physical spurious oscillations.

In the unsteady time-marching method, an implicit dual-time stepping technique [59] is employed to perform the temporal integration, where the solution is marched to steady state in pseudo-time τ . The temporal discretisation uses a 2nd order backward difference. In the steady-state approach the flow field is solved in a non-inertial reference frame with a source term and mesh velocities that account for the centripetal and Coriolis acceleration terms. This approach is valid for hovering rotors as the blade does not experience stall. Another limitation is that only flow around isolated rotors can be modelled and time-marching simulations are required if installation effects are to be considered. The harmonic balance method is described in more detail in the next subsection. For all methods the linearised system of equations is solved using the Generalised Conjugate Gradient method with a Block Incomplete Lower-Upper (BILU) factorisation as a pre-conditioner [60]. To allow an easy sharing of the calculation load for parallel jobs, multi-block

structured meshes are used [61]. For this study, the fully-turbulent Wilcox's k - ω -SST model from Menter [62] is employed.

B. Harmonic Balance Method

The harmonic balance method represents the flow solution and residual vectors as a truncated Fourier series, by assuming a periodicity in time with a frequency, ω . The flow is represented by N_H harmonic balance modes and is split into $N_T = 2N_H + 1$ subintervals, which are coupled using the Fourier collocation derivative operator, D . This leads to a significant reduction in computational costs compared to time-marching simulations, as the flow-field can be solved as a large ($N_T \times N_T$) steady state problem. A detailed description of the implementation used within the present work can be found in [42]. The harmonic balance method has also been coupled with overset grids, through the implementation of a dynamic holelist. The main problem with overset harmonic balance simulations, is the fact that a cell that is a hole (no valid solution in background grid, as solution is obtained on the foreground grid) in one snapshot can become computational in another snapshot, leading to an invalid solution. Here, to deal with the rotational movement of the rotor blades, an intermediate disk chimera level is included in the grid that rotates with the blades, keeping the cell flagging constant. The pitching and flapping motions are solved by flagging holes that dynamically change between snapshots as an interpolation cell, leading to an expansion of interpolation layers from two to an arbitrary value, which ensures that all computational cells have a valid solution. The full implementation of the overset harmonic balance method is described in [63].

C. Adjoint Method

The adjoint method offers an efficient way to produce the design variable gradients. The cost involves the solution of a stiff linear system shown in equation 4, which is similar to the cost of the baseline flow solution, independent of the number of design variables.

$$\left(\frac{\partial \mathbf{R}}{\partial \mathbf{W}} \right)^T \lambda = - \left(\frac{\partial I}{\partial \mathbf{W}} \right)^T, \quad (4)$$

The design variable gradients are obtained as follows:

$$\frac{dI}{d\alpha} = \frac{\partial I}{\partial \alpha} + \lambda^T \frac{\partial \mathbf{R}}{\partial \alpha}, \quad (5)$$

where I is the adjoint objective function, \mathbf{W} is the vector of conserved variables, \mathbf{R} is the residual vector, α is the design variable vector and λ is the adjoint variable vector.

The term $\frac{\partial \mathbf{R}}{\partial \alpha}$ for design sensitivities is obtained in the following manner:

$$\frac{\partial \mathbf{R}}{\partial \alpha} = \frac{\partial \mathbf{R}}{\partial N} \frac{\partial N}{\partial X_v} \frac{\partial X_v}{\partial X_s} \frac{\partial X_s}{\partial \alpha} \quad (6)$$

This represents the computation of the residual vector sensitivity with respect to the design variable, and is dependent on the surface mesh sensitivities with respect to each design variable $\frac{\partial X_s}{\partial \alpha}$ which are obtained from the blade parameterisation tool, the volume mesh sensitivities with respect to the surface mesh $\frac{\partial X_v}{\partial X_s}$, the mesh metrics sensitivities with respect to the volume mesh $\frac{\partial N}{\partial X_v}$ and finally, the residual sensitivities with respect to the mesh metrics $\frac{\partial \mathbf{R}}{\partial N}$.

The linear system shown in equation 4 is difficult to solve due to the high stiffness of the Jacobian matrix, $J = \partial \mathbf{R} / \partial \mathbf{W}$ (which is not stored explicitly to reduce memory demands). The present adjoint solution methodology uses a Krylov-subspace solver based on a nested GMRES solver [64] with Deflated Restating (DR), where a GMRES-DR solver is used as a preconditioner for the (outer) GMRES-DR cycles. This nested Krylov-subspace solver proved to be able to converge tough adjoint problems, as required for stiff harmonic-balance adjoint solutions. The adjoint method was developed within HMB3 through source code differentiation, using the tool TAPENADE [65]. The individual functions of the solver are differentiated and used to compute the partial derivatives required for the sensitivity equation 5. Details of the adjoint method and implementation within HMB3 can be found in [66, 67].

D. Coupling Adjoint and Overset Harmonic Balance Methods

The harmonic balance adjoint method is similar to the steady-state adjoint, however, now instead of one steady solution, the linear system is $2N_H + 1$ larger, as it contains each of the snapshots of the harmonic balance solution. The main modification of the adjoint code is the computation of the residual function, which consists of the steady residual for each of the snapshots and the effect of the Fourier collocation derivative operator. The partial derivatives $(\partial I / \partial \alpha, \partial \mathbf{R} / \partial \alpha)$ required in equation 5 are averaged over the number of snapshots to produce an averaged gradient value (same procedure as in primal solver to obtain an integrated load value). The harmonic balance adjoint method also includes the effects of mesh motion (transformations applied to the sensitivities to account for flap, pitch, lag, azimuth) and the dynamic holelist required for overset harmonic balance simulations. The present method extends the previous formulations [42, 66] to design sensitivities (rather than only aerodynamic sensitivities) for the harmonic balance method and implements coupling with the overset grid method.

E. Complete Optimisation Framework

The complete design optimisation framework is shown in Figure 1.

Firstly, the baseline flow solution is computed using the steady state solver or the harmonic balance method. The baseline objective function (I) and equality/inequality constraints (g_j and h_k respectively) are then evaluated from the

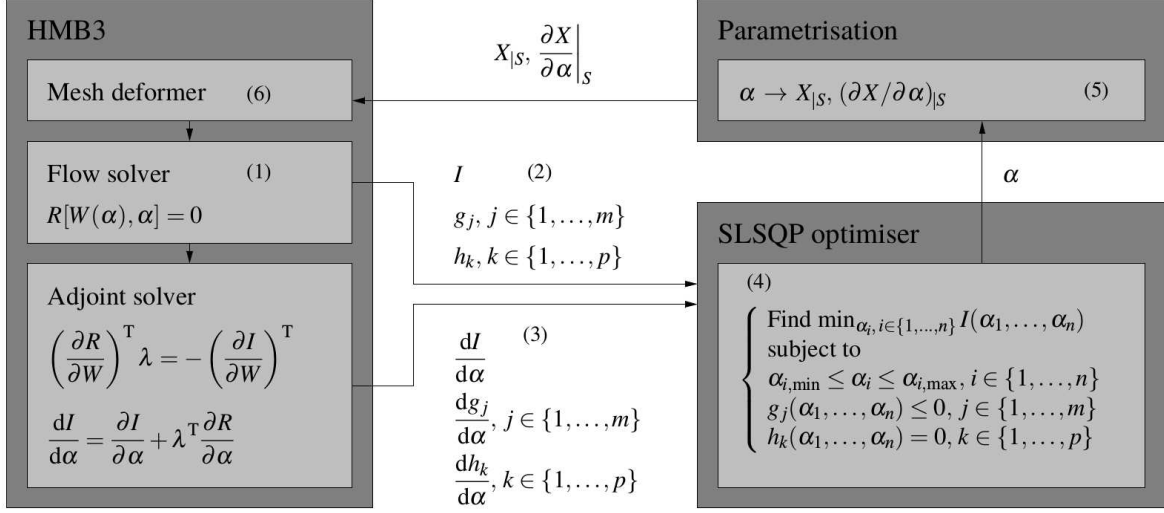


Fig. 1 The full HMB3 optimisation workflow.

base flow solution. The adjoint problem is then solved, and the design sensitivities are computed using the adjoint method. The adjoint problem may or may not be solved to full convergence to minimize computational costs, which has been verified by comparing the computed gradients with finite differences. The main aim of the adjoint method is to provide gradients which are of sufficient accuracy to drive to design in the correct direction. The cost functional, the constraints and their gradients are fed to the gradient based optimiser, to obtain a new design variable vector. In our tool chain, the Least-Square Sequential Quadratic Programming (SLSQP) algorithm [68] is used, which represents the objective function as a quadratic approximation to the Lagrangian and linear treatment of the constraints. The updates of the Hessian matrix approximation are based on the Broyden-Fletcher-Goldfarb-Shanno (BFGS) algorithm [69]. Based on the new vector of design variables the surface to be optimised is deformed based on an external parameterisation tool (details in next subsection). The parameterisation outputs the coordinates of the new surface as well as the surface sensitivities which are used in the adjoint method. Finally, a mesh deformation algorithm based on Inverse-Distance Weighting (IDW) is employed to update the volume mesh. The optimisation workflow loop is continued until a stopping criterion is reached, which is in this case is either an update tolerance on the objective function or the design variables.

F. Blade Surface Parameterisation

A deformative blade surface parameterisation method is used, where the movement of the blade surface mesh points is described analytically, and the volume mesh is updated using an IDW method. The twist law is parameterised using a Bernstein polynomial function [70] with seven coefficients. The chord is altered at four radial stations of $r/R = 0.5, 0.75, 0.943$ and 1.0 ; whereas the sweep and anhedral angles are changed at the three outboard radial stations of $r/R = 0.75, 0.943$ and 1.0 . Linear distributions are imposed inboard of 0.943 , with parabolic distributions of the blade

chord, sweep and anhedral angles across the blade tip region from $0.943 R$ to $1.0 R$. This leads to a total of 17 design parameters. The aerofoil sections at each radial station were kept fixed. The blade planform parameterisation is shown graphically in Figure 2. For the parameterised AH-64A planform, the differences between the sweep at the trailing edge and leading edge are neglected (both initiated from $r/R=0.943$).

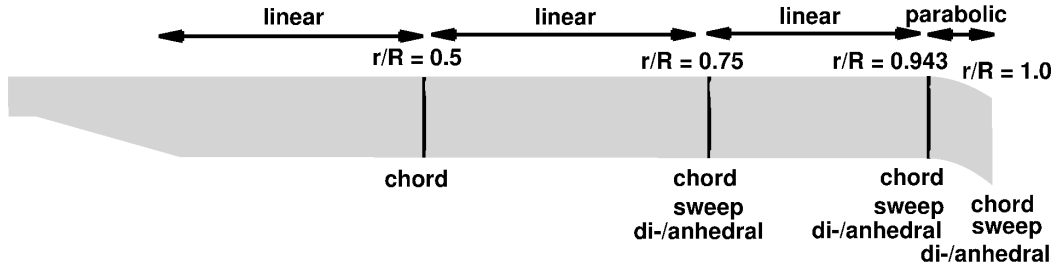


Fig. 2 Blade surface parameterisation used for the AH-64A optimisation study.

As a deformative method is used, the parameters are applied as a delta to the baseline surface mesh. Here, the blade tip sweep is removed before applying the new set of parameters, hence a rectangular blade with -9 degrees linear blade twist is used. The design parameter boundaries are shown in Table 1.

Table 1 Design parameter upper and lower boundaries for the optimisation of the AH-64A blade in hover.

Design Parameter	Boundary values
TWIST1 - TWIST7	$\pm 5 \text{ deg}$
CHORD at $r/R = 0.5$	$[0.8c, 1.4c]$
CHORD at $r/R = 0.75$	$[0.8c, 1.4c]$
CHORD at $r/R = 0.943$	$[0.8c, 1.4c]$
CHORD at $r/R = 1.0$	$[0.3c, 1.5c]$
SWEEP at $r/R = 0.75$	$[-0.3c, 0.4c]$
SWEEP at $r/R = 0.943$	$[-0.3c, 0.4c]$
SWEEP at $r/R = 1.0$	$[-0.7c, 0.4c]$
ANHEDRAL at $r/R = 0.75$	$[-0.1c, 0.25c]$
ANHEDRAL at $r/R = 0.943$	$[-0.1c, 0.25c]$
ANHEDRAL at $r/R = 1.0$	$[-0.25c, 0.1c]$

III. Blade Geometry and Computational setup

A. Blade geometry

To demonstrate the developed optimisation framework, the AH-64A rotor blade was selected. This rotor blade has sufficient information in open-literature [9, 71, 72] to perform validation studies and then optimise the planform. The AH-64A blade was also chosen as it operates on a highly-loaded helicopter. The AH-64A rotor blade geometry

was built based on the information provided for the model scale blade by Berry [72] and the rotor design paper by JanakiRam et al. [9]. The model scale (0.27) rotor blade planform is shown in Figure 3, although all simulations within this paper were performed for the full-scale rotor blade. The AH-64A rotor blade has a swept tip, a linear blade twist of nominally -9 degrees and an aspect ratio of 13.714. The blade is composed of two aerofoil sections, the HH-02 section up to 0.943R and the NACA64A006 section at the tip of the blade. Information about the aerodynamic characteristics of these aerofoils can be found in [73] and [74] respectively. Details of the geometric uncertainties can be found in [63].

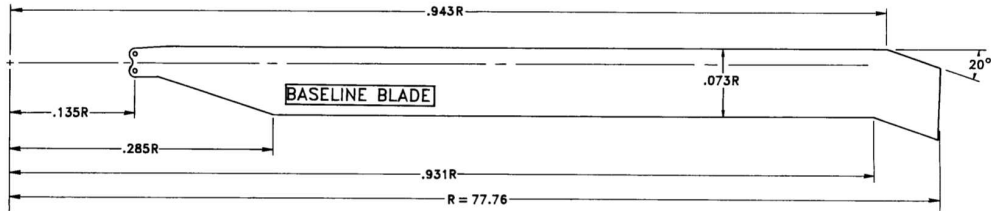


Fig. 3 Planform of the AH-64A blade based on the 0.27 scale blade [72]. Radius dimension given in inches

B. Computational setup

All simulations are performed for isolated and rigid rotors to reduce the computational costs. In hover, a steady state formulation is used, and only a quarter of the computational domain was meshed, assuming periodic conditions for the flow field in the azimuthal direction. This assumption is valid if the wake generated by the rotor is assumed periodic and the blades do not experience deep stall. A source/sink model, first introduced by Srinivasan et al. [75], is used for the simulations with Froude boundary conditions imposed at the inflow and outflow. A typical computational domain for hover simulations is shown in Figure 4 a). The distances between the rotor blades and the inflow/outflow surfaces are based on experience from previous studies using the HMB3 solver [54]. In forward flight, the full rotor disk is modelled for both time-marching and harmonic balance simulations with four blades as the flow is highly unsteady. A 0.5 degree time-step is used for time-marching calculations. The hub is modelled as a generic ellipsoidal surface. The flow is solved in a cylindrical domain with farfield boundary conditions. The rotor blade foreground grid is inserted into an intermediate background rotor disk that rotates with the blades to ensure a constant chimera holelist due to rotation of the blades in azimuth. A adiabatic boundary condition is used at the solid boundary, and the geometric conservation laws are not directly enforced with an analytical computation of the grid velocities. A matrix trimming routine is used to achieve the target thrust coefficient whilst minimizing the pitching and rolling moments [54].

A multi-block structured mesh is generated for the AH-64A rotor blade simulations using ICEM-HEXA. The chimera technique is used, hence a foreground grid was generated to resolve the blade geometry, with a background grid to capture the farfield wake geometry. This type of method allows for grid deformation, due to blade flapping and pitching in forward flight, without affecting the grid quality. For the blade foreground grid, a C topology around

the leading edge, was selected, whereas a H-topology is employed behind the trailing edge. The baseline foreground topology is shown in Figure 4 (b). The cylindrical background grid employs grid stretching to reduce the mesh size. The approximate background cell size for the first vortex passage is approximately 5% of the blade chord **for the baseline grid**. In hover, the same grid was used for CFD validation and the optimisation process, whereas a coarser grid is used for forward flight optimisation due to memory requirements of the adjoint harmonic balance method. The grid details and sizes are described in Table 2. **The wall distance of $1.0 \cdot 10^{-6} c_{\text{ref}}$ corresponds to a y^+ of 0.55 (based on hover blade tip velocity).**

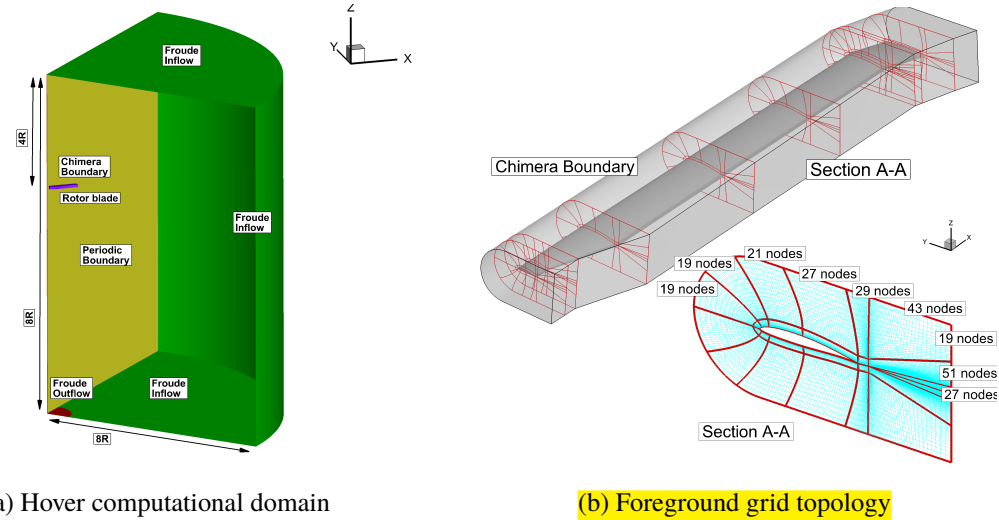


Fig. 4 Computational setup for the AH-64A blade in hover including the computational domain and foreground grid topology.

Table 2 Grid details and sizes for the AH-64A rotor blade grids in hover and forward flight. **H= Hyperbolic.**

Grid	Hover grid Baseline	Forward flight	
		Baseline	Coarse
Around aerofoil (nodes)	230	230	182
Blade normal (nodes)	70	70	56
Blade spanwise (nodes)	165	165	109
Wall distance	$1.0 \cdot 10^{-6} c_{\text{ref}}$	$1.0 \cdot 10^{-6} c_{\text{ref}}$	$1.0 \cdot 10^{-6} c_{\text{ref}}$
Chimera boundary spacing	5%cc	5%cc	10%cc
LE spacing (expansion ratio)	0.0005c, H (1.12)	0.0005c, H (1.12)	0.0005c, H (1.12)
TE spacing (expansion ratio)	0.0001c, H (1.24)	0.0001c, H (1.24)	0.0002c, H (1.4)
Foreground (cells)	5.4M	21.6M(4 × 5.4M)	9.5M (4 × 2.375M)
Background (cells)	5.3M	14.5M	3.6M
Total (cells)	10.7M	36.1M	13.1M

C. Test conditions

All computations are performed for a blade tip Mach number of 0.65 and Reynolds number of 7.98×10^6 based on the blade tip velocity and chord of the first aerodynamic section (0.5334m). The Reynolds number is not updated during the optimisation process. The computed test conditions are shown in Table 3.

Table 3 Conditions of the simulations performed within the AH-64A validation and optimisation process.

Computation	Conditions
Hover validation	Collective sweep: $6^\circ, 8^\circ, 10^\circ, 11^\circ$
Forward flight validation	$C_T = 0.00903, \mu = 0.2, 0.3$
Hover optimisation	Fixed collective: 11°
Forward flight optimisation	$C_T = 0.00903, \mu = 0.3$

For the CFD validation, the conditions were selected based on available experimental data [9, 71]. The hover and forward flight optimisation studies were performed at high-thrust due to constantly growing payload requirements [9]. The baseline validation case was used for the forward flight optimisation as a demonstration of the developed overset harmonic balance adjoint optimisation framework.

IV. CFD Validation

Before moving to the optimisation results, CFD validation of the HMB3 solver is presented for the AH-64A rotor blade in hover and forward flight. Where, available comparisons are made with experimental data [9, 71]. An assessment is also made of the baseline AH-64A blade design.

A. Validation of steady-state and time-marching solvers

Firstly, the performance predictions in hover and forward flight for baseline AH-64A are validated against experimental data [9, 71]. Hover test data is from whirl tower tests, whereas the forward flight data is equivalent to the YAH-64 flight test data. The integrated load predictions are compared with experimental data in hover and forward flight and shown in Figure 5.

Very good performance predictions are obtained in hover, when compared with whirl tower test data, with CFD predictions at the upper bound of the test data scatter. In forward flight, slightly higher uncertainties exist because only engine power is available from flight tests. These values need to be corrected for tail rotor power, auxiliary power and transmission losses to obtain main rotor power. The CFD main rotor power values, however, are below the test data, which after a correction of 8% (as used in [76]) lead to excellent agreement with the test data. The harmonic balance solver has also been validated for the AH-64A blade in forward flight with results presented in [63].

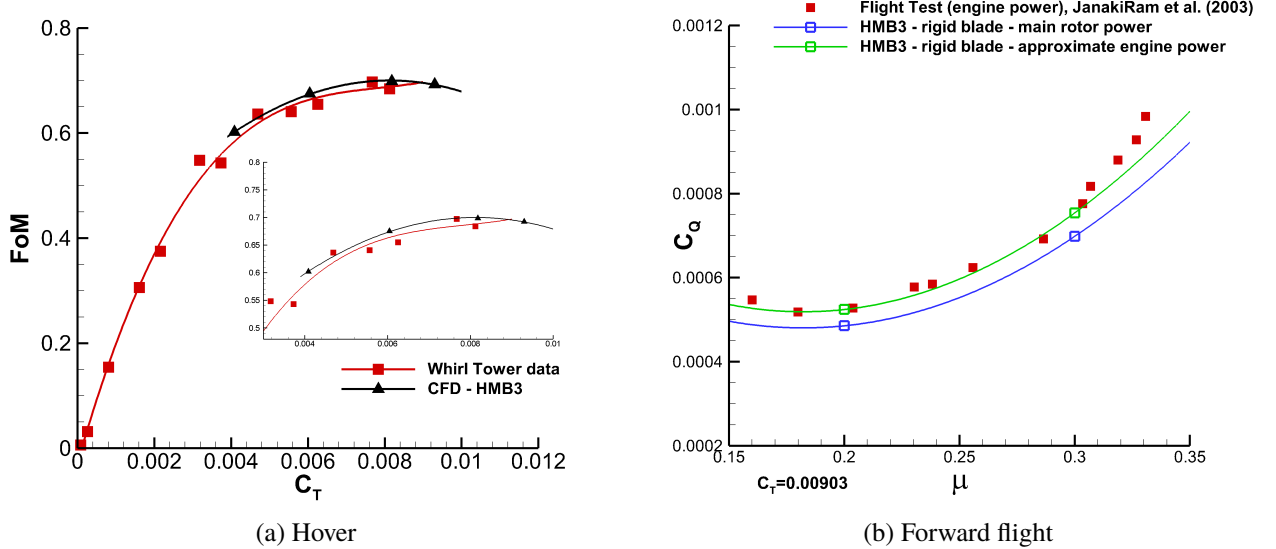


Fig. 5 Comparison of the CFD performance predictions for the baseline AH-64A rotor blade with experimental data [9, 71].

B. Assessment of the baseline AH-64A blade design

Based on the CFD validation calculations in hover and forward flight, the AH-64A blade design can be assessed.

Firstly, the surface pressure distribution in hover at 11° collective is shown in Figure 6.

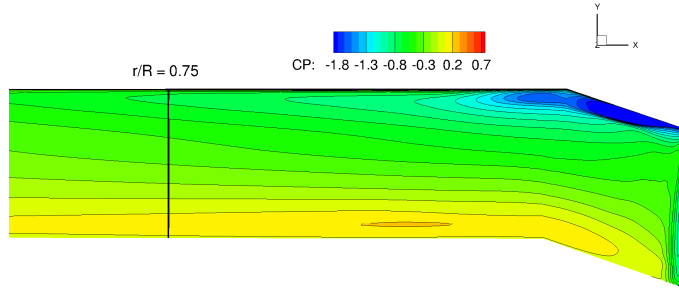


Fig. 6 AH-64A rotor blade surface pressure distribution in hover at 11° collective.

The surface pressure distribution indicates the formation of a strong shock near the blade tip at the leading edge. This feature would lead to a significant increase in power requirements, and could potentially be weakened through an optimisation study. Additionally, the pressure is not fully-recovered at the trailing edge, indicating the onset of blade stall.

The forward flight features of the AH-64A rotor blade at $C_T = 0.00903, \mu = 0.3$ are shown in Figure 7.

The AH-64A rotor blade also exhibits adverse flow features in forward flight. A shock is observed on the advancing side, and the flow is supersonic over a large portion of the blade chord. The wake visualisation indicates the presence of dynamic stall on the retreating side as the vortex from the back of disk interacts with the retreating side blade. This

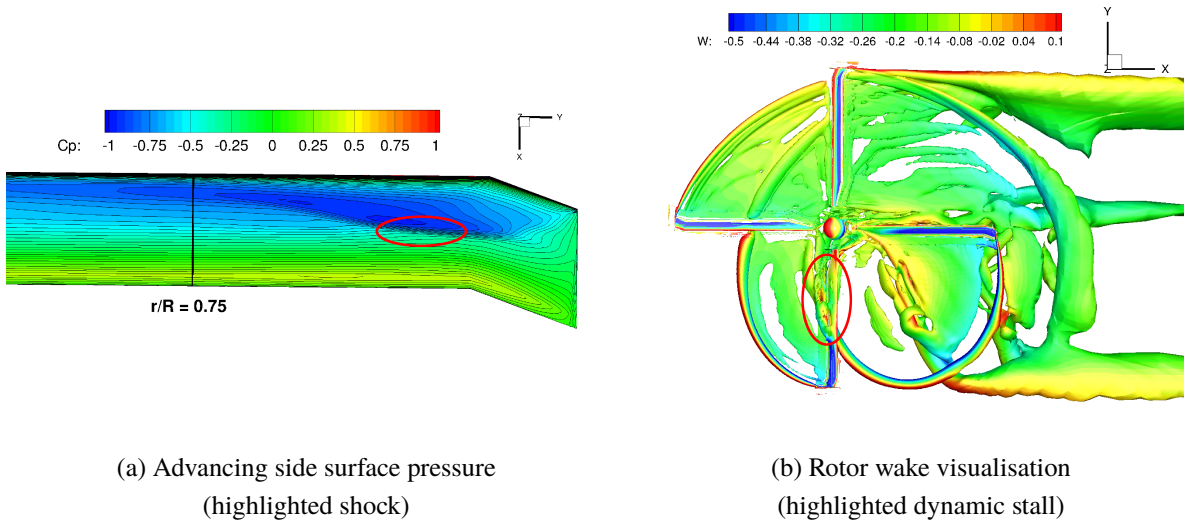


Fig. 7 Forward flight advancing side surface pressure distribution and rotor wake visualisation using Q-criterion (value of 0.002) coloured by downwash velocity for the AH-64A rotor blade at $C_T = 0.00903, \mu = 0.3$.

interaction causes dynamic stall which will lead to an increase in rotor power required as well as having a large effect on the local pitching moments, leading to high control loads. The adverse flow features present for the baseline AH-64A rotor blade design make it a good case to exercise the optimisation framework, as the design can clearly be improved through reducing the shockwave and dynamic stall features.

V. Rotor Blade Optimisation

The optimisation is demonstrated for the AH-64A rotor blade in this section. Firstly, the blade is optimised in hover. Based on the hover-optimised blade, an optimisation in forward flight is carried out, whilst keeping the key design features that lead to the hover performance improvement. Finally, the new design is validated by performing time-marching calculations on a finer mesh.

A. Optimisation in hover

Firstly, the AH-64A rotor blade is optimised in hover using the steady-state adjoint formulation. The steady-state adjoint can be used here, as the flow does not exhibit deep stall, and can be treated as steady. Alternatively, the harmonic-balance adjoint method could have been used with one harmonic balance mode, leading to an increase in computational resources, with the same expected result. The same grid is used as for the CFD validation of the baseline AH-64A blade. A high thrust condition is selected (fixed collective of $\theta_0 = 11^\circ$ corresponding to $C_T = 0.0093$). The objective function is set to minimize power with a constraint on the thrust. This formulation allows to keep the rotor blade thrust-weighted solidity as a free parameter, as opposed to a FoM optimisation, where solidity needs to be kept constant. The blade surface parameterisation includes blade twist, chord, sweep and anhedral parameters as described

in Section II. F. 1, giving a total of 17 design variables. The parameterised AH-64A rotor blade is slightly different than the baseline blade as shown in Figure 8. The design histories of the thrust coefficient, torque coefficient and Figure of Merit are shown in Figure 9.



Fig. 8 Difference between the baseline (grey) and parameterised (red) AH-64A blades.

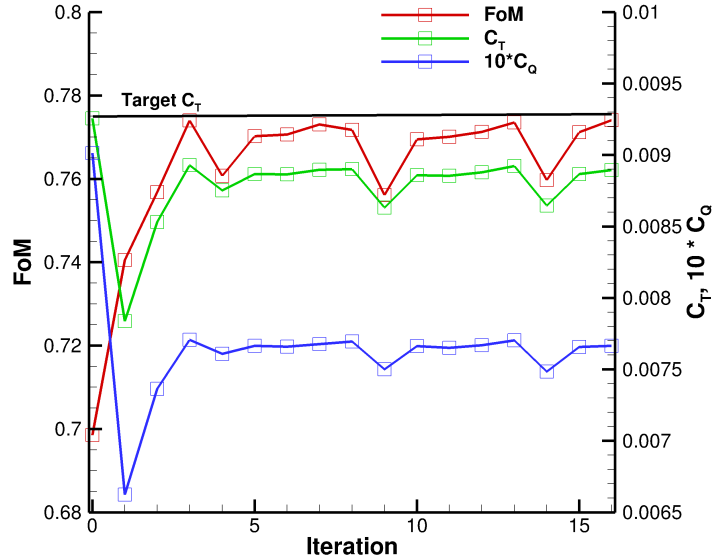


Fig. 9 History of the integrated loads with each iteration.

The optimisation history shows that a near optimal blade was obtained after three design iterations. The optimiser then tries to further minimize the power, but goes further away from the target thrust and follows up by reverting to a similar design. The thrust constraint is not fully met due to the highly nonlinear design space and a tolerance imposed on the constraint function. The optimised shape is compared to the baseline AH-64A blade in Figures 10-11.

The new blade design has the maximum available blade twist with the upper and lower bounds reached at the blade root and tip respectively, leading to a linear blade twist of -19 degrees. A forward-backward swept blade shape is obtained with a significantly higher planform area than the baseline blade design. This is due to the imposed thrust constraint at a fixed collective. The increase in solidity is therefore, a result of the thrust constraint, and is not driven by the optimiser to increase hover performance. The interaction between the optimum planform shape and the collective

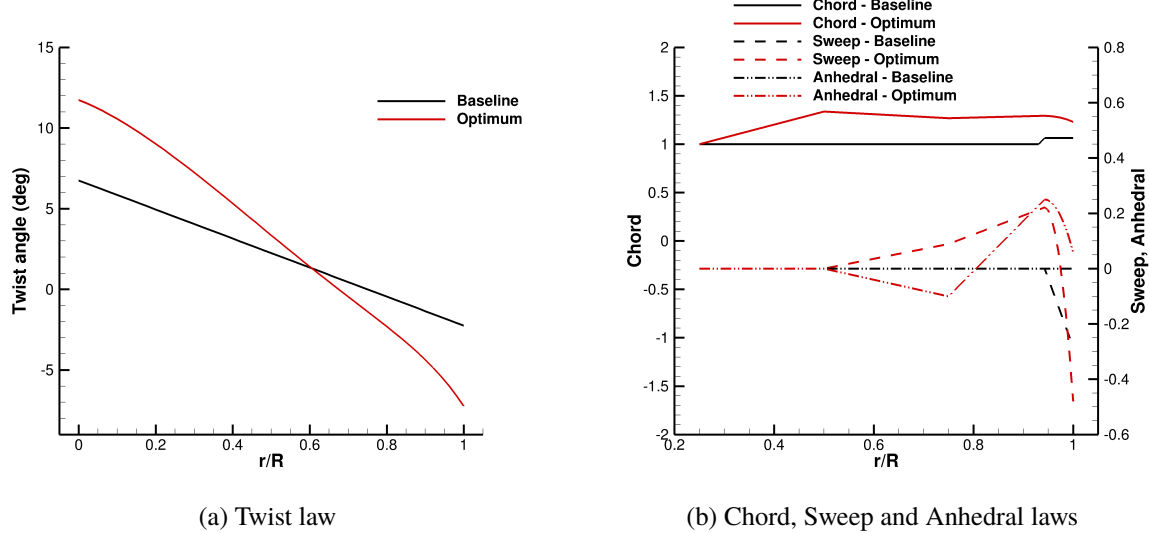


Fig. 10 Comparison of baseline AH-64A and hover optimised geometric laws. Chord, Sweep and Anhedral values given based on a unit chord length (chord of first aerodynamic section).

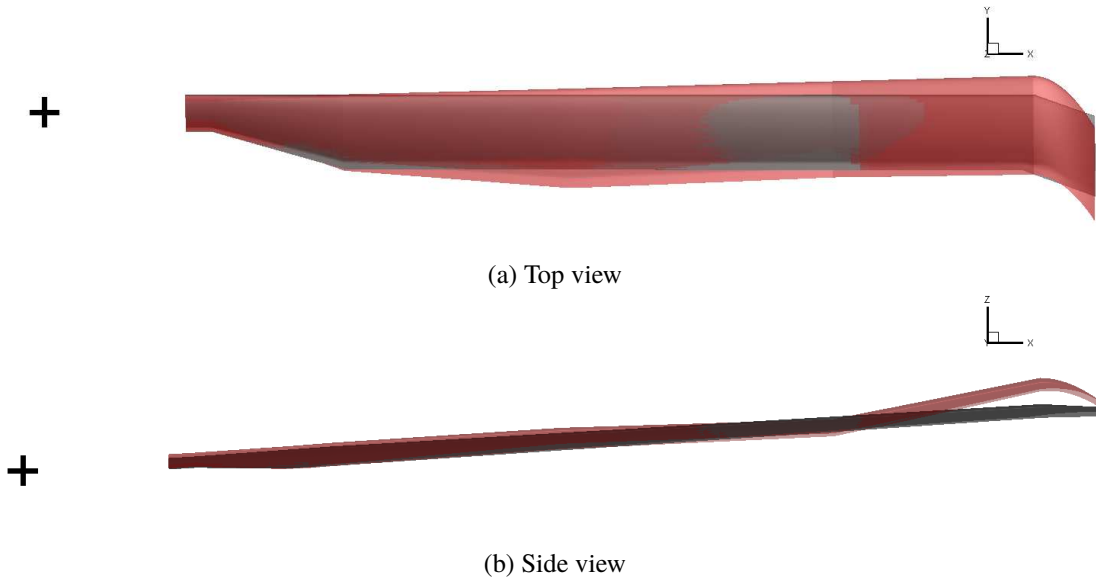


Fig. 11 Comparison between the baseline (grey) and optimum (red) planform shapes for the AH-64A rotor blade in hover at 11 deg collective.

angle should be examined further, as part of future work. The blade design also has a distinct dihedral-anhedral shape to minimize the interaction of the blades with the preceding blade tip vortices. The integrated loads for the baseline and optimised designs are shown in Table 4.

A benefit of 7.8 counts (0.01 = 1 count) is seen in Figure of Merit for the optimised blade design. A slightly lower thrust coefficient is seen during the optimisation process, hence the blade is re-trimmed to the required thrust. This leads to a benefit of 8.9 counts in Figure of Merit at the thrust of the baseline blade. Based on the design gradients,

Table 4 Comparison of the integrated loads between the baseline, parameterised and optimum AH-64A planforms in hover

Planform	θ_0	C_T	C_Q	FoM	FoM difference
AH-64A Baseline	11.0	0.00930	0.000911	0.696	-
AH-64A Parameterised	11.0	0.00925	0.000901	0.699	+0.3 counts
AH-64A Optimised	11.0	0.00890	0.000766	0.774	+7.8 counts
AH-64A Optimised (re-trimmed)	11.194	0.00929	0.000807	0.785	+8.9 counts

the largest contributors to the increase in the hover performance are the dihedral-anhedral planform shape and the high blade twist. The exact shape of the planform is of less importance in hover conditions. The surface pressure distributions for the baseline and optimised blades are shown in Figure 12.

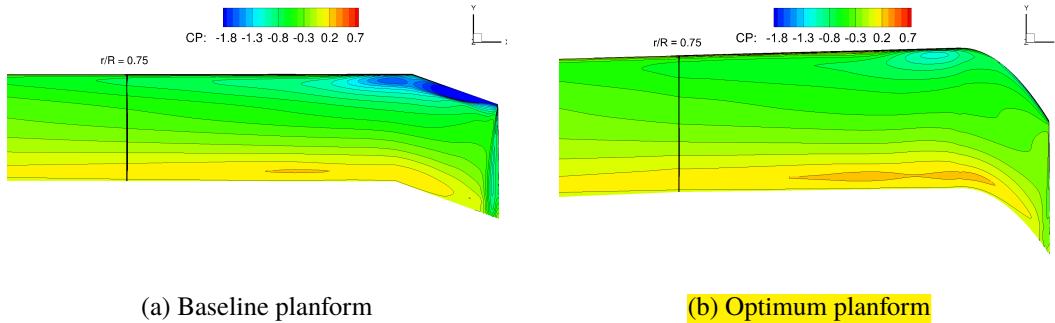


Fig. 12 Surface pressure distributions for the baseline and optimised AH-64A rotor blades at $C_T = 0.0093$.

The baseline AH-64A blade has a strong shockwave at 11 degrees collective, which is completely removed for the optimised blade. The new planform shape offloads the blade tip, shifting the load further inboard, leading to a more optimal surface pressure distribution and hence higher performance. This is further confirmed by the sectional load distributions shown in Figure 13.

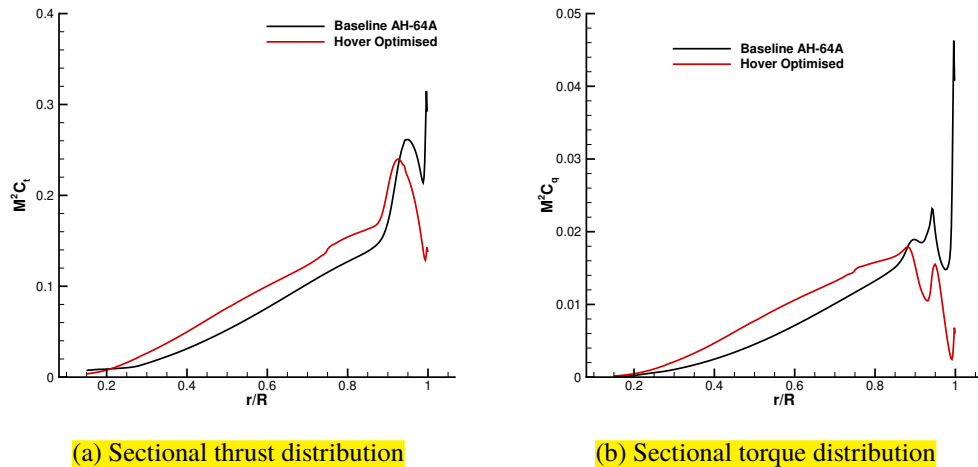


Fig. 13 Sectional loads for the baseline and hover optimised AH-64A rotor blades at $C_T = 0.0093$.

The sectional loads show a significantly higher loading inboard and an offloaded blade tip. This leads to a more optimal loading distribution, and thus leading to a much higher Figure of Merit. Finally, the vortical structures are visualised in Figure 14.

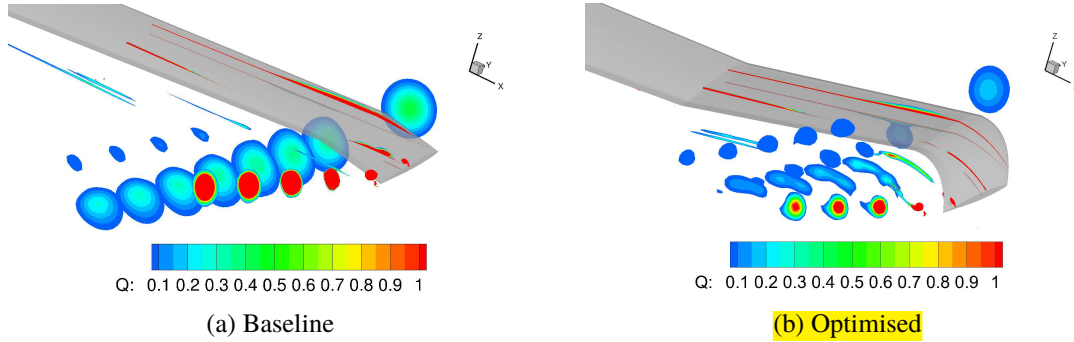


Fig. 14 Blade tip vortices visualised by contours of Q-criterion (cut-off value of 0.05) for the baseline and optimised AH-64A planforms at $C_T = 0.0093$.

The offloaded blade tip produces a much weaker tip vortex, mainly due to the high blade twist and sharp blade tip anhedral. The distinct non-planar dihedral-anhedral shape minimizes the interaction of the blade vortex with the next blade. A discontinuity in the blade shape, however, leads to the shedding of an additional vortical structure where the anhedral starts.

B. Optimisation in forward flight

The AH-64A blade is also optimised in forward flight using the harmonic balance adjoint framework. The moderate advance ratio, high lift condition of $\mu = 0.3$, $C_T = 0.00903$ used for CFD validation is selected for the optimisation study. In this case, a coarser grid of 13.1M cells is used with two harmonic balance modes. As a four-bladed rotor was used, this leads to a rotor solution snapshot every 18 degrees, with a full capturing of viscous and unsteady wake effects. The starting point for the optimisation process was a rectangular blade with the aerofoils of the AH-64A blade and the dihedral-anhedral distribution of the hover optimised blade. This design feature was carried on through to the forward flight design process as it was the main characteristic of the hover optimised blade that led to hover performance improvements. The blade twist, although a parameter that has a large impact on hover performance, was set as a free parameter in forward flight, as such a high blade twist could lead poor performance in forward flight. The same parameterisation was used as in hover, with the anhedral/dihedral parameters kept fixed, leading to 14 design parameters. As the twist design variable gradients were much larger than the other parameters due to radians used as units ($5 \text{ deg} = 0.0872665$), the twist design variable bounds were rescaled to $<-0.8,+0.8>$, giving these design variable values of similar order as the other design parameters, leading to improved convergence of the optimiser. The adjoint problem is not fully converged to minimize the computational costs, however, the obtained gradients have been proven to drive the design in the correct direction, as verified through finite differences. The optimisation problem was setup

the same way as for hover optimisation, hence the objective function was to minimize power whilst constraining thrust. The shape updates in forward flight, however lead to pitching and rolling moments which disturb rotor trim. To account for trim state changes, a semi-trim strategy was adopted where the rotor was trimmed to the initial thrust coefficient of the new design (typically lower than $C_T = 0.00903$) whilst minimizing pitching and rolling moments. This procedure drove the optimisation process in the correct direction, and ensured that the shape is updated based on both the thrust constraint and power objective. The differences in the trim state between design iterations, outside the optimiser algorithm, led to inaccuracies in the SLSQP Hessian matrix update. For this reason, every few optimiser iterations, the design was re-trimmed to the target thrust of $C_T = 0.00903$, the Hessian matrix was discarded and the optimisation process was restarted. As the optimisation process did not impose any constraints on the pitching and rolling moments, it cannot be stated with full confidence whether the optimiser was driving the design to a better aerodynamic shape or design with pitching and rolling moments that reduce the rotor power. This is one of difficulties associated with forward flight rotor optimisation, as the rotor power is actually more sensitive to the rotor trim state rather than the rotor shape. However, the strategy adopted here was proven to be successful in generating better designs after full re-trimming.

The final design was obtained after 20 design iterations, with the optimisation restarted three times at iterations 3, 11 and 17, by re-trimming the blade to $C_T = 0.00903$ and discarding the approximate Hessian. In all other iterations, the design was trimmed to the new design thrust with minimised pitching and rolling moments. The optimised design led to a power improvement of 5.1% compared to the baseline AH-64A blade, which is significant given that the same aerofoil sections were kept. The final design is analysed in more detail with the geometric laws and planform shape shown in Figures 15-16.

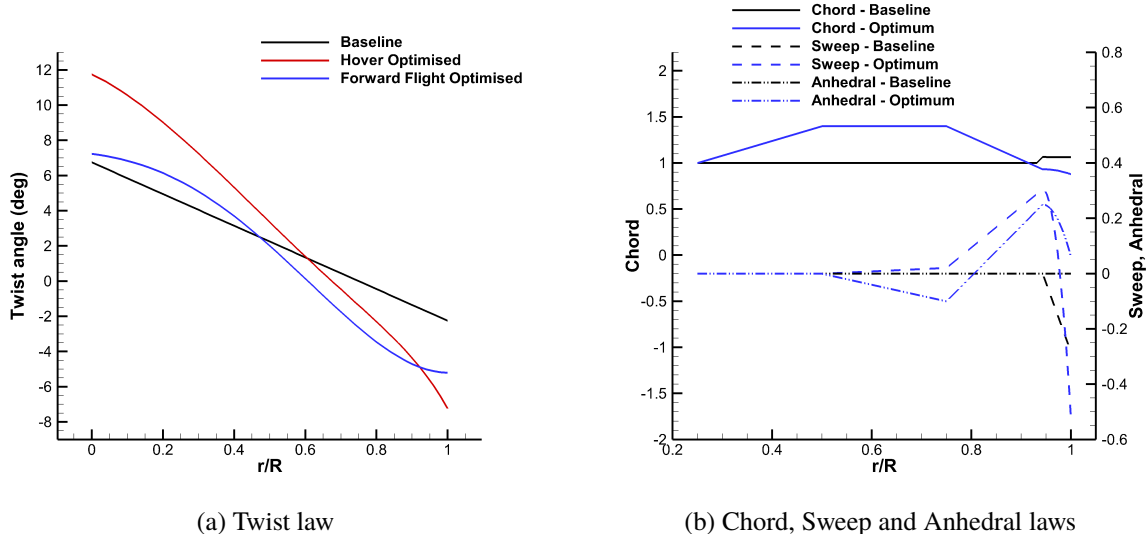


Fig. 15 Comparison of baseline AH-64A and forward flight optimised geometric laws. Chord, Sweep and Anhedral values given based on a unit chord length (chord of first aerodynamic section).

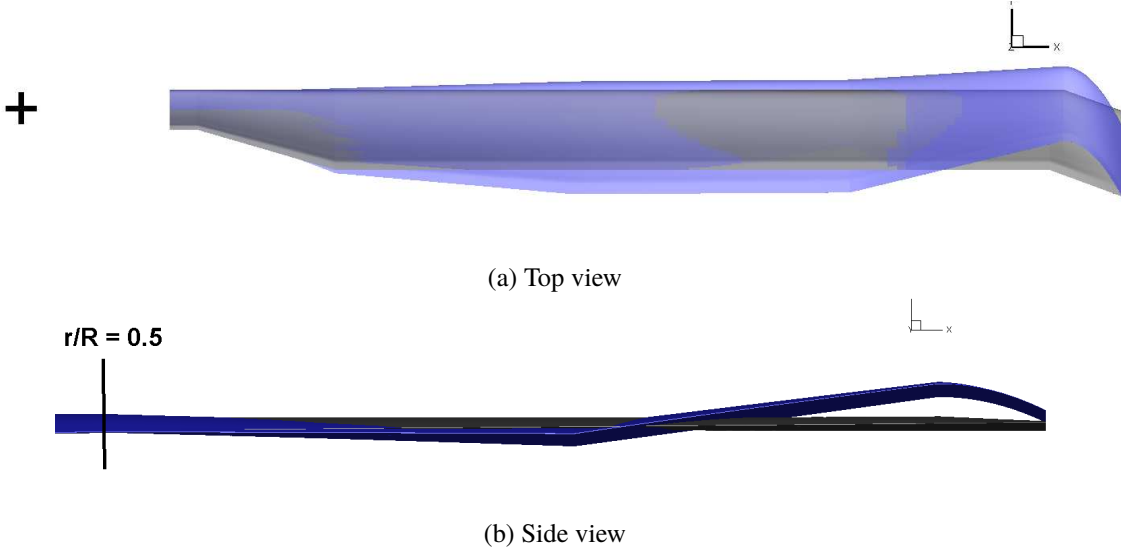


Fig. 16 Comparison between the baseline (grey) and forward flight optimised (blue) planform shapes for the AH-64A rotor blade in forward flight at $C_T = 0.00903$, $\mu = 0.3$.

As in hover, the optimiser leads to a forward flight design with increased blade twist compared to the baseline AH-64A blade. The blade twist is similar to the hover optimised blade in the region of $r/R=0.5$ to $r/R=0.8$, and flattens out towards the blade tip, leading to an increase in tip loading. The inboard twist is similar to the baseline design. The chord distribution leads to a planform with maximum chord inboard, with a significantly reduced tip area, leading to a reduction in both profile and induced power through a more favourable blade loading. The forward flight optimised blade also has a forward-backward sweep distribution, which is more aggressive when compared to the hover optimised design, mainly aimed at reducing compressibility effects. It must, however, be noted that no integrated pitching moment constraints were present in the optimisation process, hence the blade may not be fully balanced in pitch. The dihedral-anhedral distribution is retained from the hover design, however, based on the design gradients, blade tip dihedral seems to be more favourable in forward flight. This would, however, potentially lead to a reduction in the blade hover performance. The exact planform shape may be influenced by the semi-trim strategy and non-inclusion of the control angles as design variables. The optimisation may have been guided by the generation of favourable pitching and rolling moments. In particular, highly twisted blades, have lower longitudinal cyclic requirements leading to a more uniform angle of incidence across the rotor disk. In the present optimisation study, the main feature used to recover the thrust loss due to high twist and lower tip area, was a large inboard chord. A slightly different optimal design may be found, for example at a higher collective, but lower planform area. In the future, the planform should be optimised together with the trim state. However, despite, the fact that the trim state variables were not included within the optimisation process, the final design still yields a 5.1% power benefit over the baseline blade. The source of the performance improvements is examined further, based on the harmonic balance solutions, by extracting the rotor disk loads shown in Figure 17. A comparison is made between the baseline parameterised AH-64A blade (with a parabolic

blade tip) and the forward flight optimised blade. The loads are scaled by a reference chord equal to the chord of the first aerodynamic section (unit chord in simulation corresponding to 0.5334m in real-life). The M^2C_l and M^2C_d represent force values normal and tangential directions (non-radial) to the rotor disk plane representing the local lift and drag values uncorrected for downwash effects (hence, thrust and torque/(local radius)).

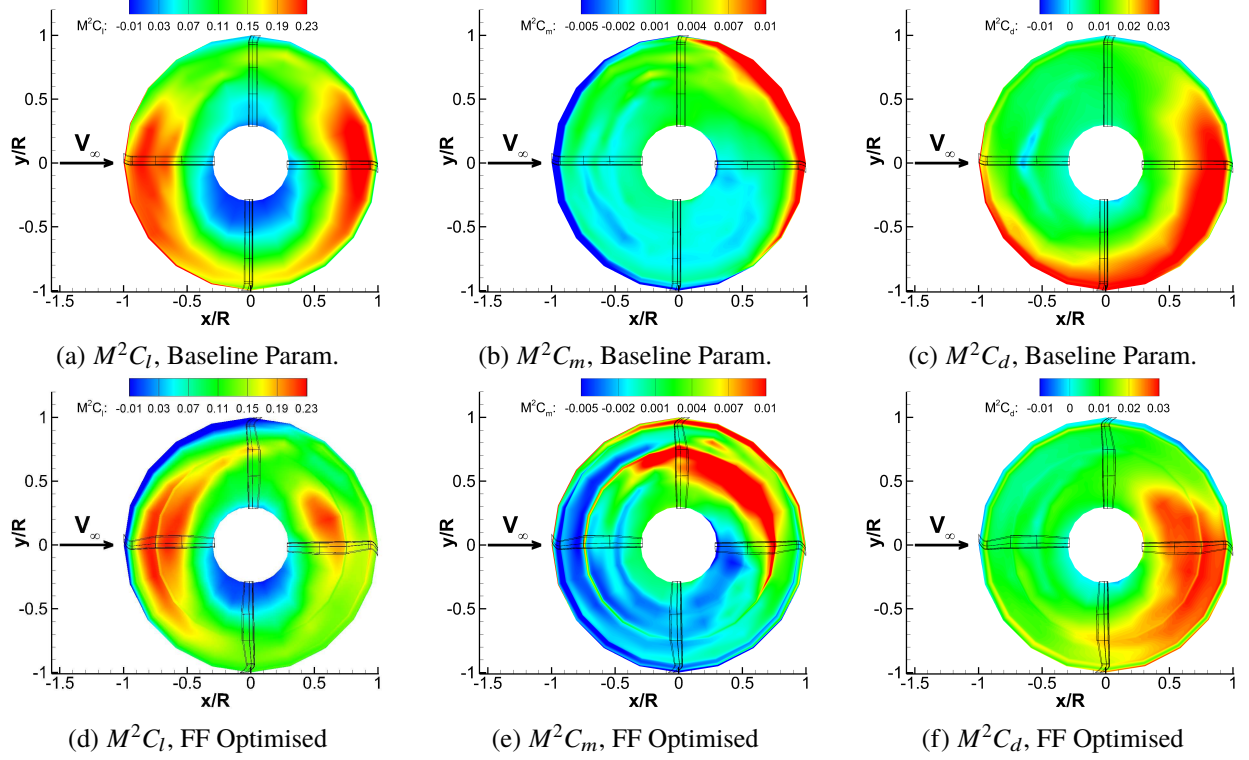


Fig. 17 Comparison of the rotor disk loads for the baseline parameterised (with parabolic blade tip) and forward flight optimised AH-64A rotor blades in forward flight at $C_T = 0.00903$, $\mu = 0.3$ based on 2 mode harmonic balance solutions.

Comparing the lift force rotor disk distributions, the most obvious features is a significantly offloaded tip for the forward flight optimised blade. This can especially be seen at the back of the rotor disk and on the advancing side. This is also an action of the change trim state, as the lateral cyclic is increased, leading to higher tip loading at the back of the rotor disk and lower tip loading at the front of the rotor disk. The loading is also increased inboard at the front and back of the rotor disk, whereas, the retreating side loading is significantly reduced. A minor discontinuity can also be seen in the loading as well as pitching moments at $r/R=0.75$ caused by the sharp introduction of the blade dihedral. In general a greater pitching moment variation is seen for the optimised blade, especially inboards of the blade tip. The in-plane force loading shows a significantly reduced drag force across the blade tip at all azimuthal stations, which is especially visible at the front of the rotor disk and on the retreating side. At the back of the rotor disk, the region of high chordwise force shifts inboard, following the lift force trends. Based on the harmonic balance solutions, the performance improvement is mostly coming from a redistribution of the loading inboard and offloading of the blade

tip. This loading distribution also increases the lateral cyclic but leads to a reduction in the longitudinal cyclic, leading to a power reduction due to a more uniform angle of incidence across the rotor disk. The trim state differences are analysed further in the next section, based on time-marching calculations.

C. Validation of the new blade design

The new blade design is simulated in hover and forward flight on a finer grid. The dihedral-anhedral shape was also smoothed out where sharp changes in curvature were seen, by using a third order Bezier curve between $r/R = 0.75$ and $r/R = 0.943$ as shown in Figure 18. The integrated load results are shown in Table 5.

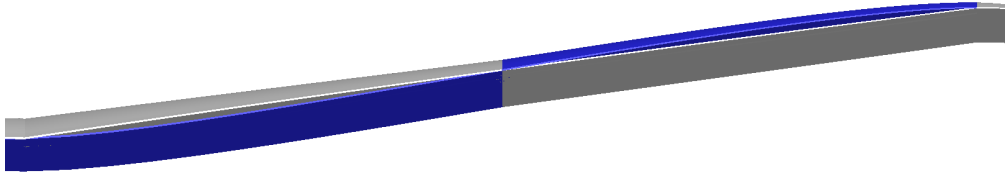


Fig. 18 Smoothed anhedral distribution using a 3rd order Bezier curve between $r/R = 0.75$ and $r/R = 0.943$. Baseline shown in grey and smoothed distribution shown in blue.

Table 5 Comparison of the integrated loads in hover ($C_T = 0.0093$) and forward flight ($\mu = 0.3$, $C_T = 0.00903$) between the baseline (BASE) and forward flight optimised (FF OPT) AH-64A planforms based on time-marching simulations. Value in brackets represents performance benefit over baseline blade. A breakdown of the forward flight pressure (C_{Qp}) and viscous (C_{Qv}) torque components is also given.

Hover		
	BASE	FF OPT
FoM	0.696 (-)	0.757 (+6.1 counts)
C_T	0.00930	0.00928
θ_0	11.0	12.403
Forward flight		
C_T	0.00906	0.00904
C_Q	6.984×10^{-4} (-)	6.529×10^{-4} (-6.51%)
C_{Qp}	6.097×10^{-4}	5.462×10^{-4}
C_{Qv}	8.870×10^{-5}	1.066×10^{-4}
C_{Mx}	3.454×10^{-6}	-2.703×10^{-6}
C_{My}	2.045×10^{-5}	-3.523×10^{-6}

The hover performance is significantly improved compared to the baseline blade, as a benefit of 6.1 counts in FoM is obtained at $C_T = 0.0093$. The hover performance is slightly deteriorated when compared to the hover optimised blade (8.9 counts benefit), however, the forward flight optimised blade also leads to a 6.5% improvement in forward flight. The forward flight design has an offloaded blade tip compared to the baseline AH-64A blade, through the introduction of a non-linear twist distribution, along with a forward-backward sweep distribution leading to a further reduction in

the pressure torque term. The viscous torque term is slightly increased due to dihedral-anhedral distribution leading to a more non-planar planform along with the higher inboard chord. The performance improvement obtained through time-marching calculations is slightly higher than the optimisation result, due to differences between time-marching and 2 mode harmonic balance simulations as well as grid sizes (13.1M vs 36.1M cells). The harmonic balance calculations tend to overpredict the turbulent eddy viscosity levels in the wake compared to the time-marching calculations leading to reduced performance improvements between designs (to overcome this, a higher number of modes would be required). Differences are also seen in the trim states, shown in Table 6. All calculations were within 1% of the required thrust and had close to zero pitching and rolling moments. The trimming routine used a fixed shaft angle of 5.341° , coning angle of 3.5° and zero flapping.

Table 6 Differences in trim state, between the baseline and forward flight optimised designs as well as time-marching (TM) and 2 mode harmonic balance (HB) calculations. Note: Negative Fourier series used.

Case	θ_0	θ_{1s}	θ_{1c}
Baseline (TM)	10.413	7.421	-3.072
Baseline (HB)	10.873	7.904	-2.943
Forward Flight Optimised (TM)	11.330	6.359	-3.855
Forward Flight Optimised (HB)	11.913	6.996	-3.599

As can be seen in Table 6, the time-marching and harmonic balance calculations have differences in trim state of approximately 0.5-0.6 degrees in collective and longitudinal cyclic. A more extreme trim state is predicted by the harmonic balance calculations, which may reduce (in this case) the obtained performance benefits. Another aspect to highlight is the higher collective required by the forward flight optimised blade compared to the baseline blade to achieve the target thrust. This is due to the significantly reduced blade tip area and increased blade twist leading a reduced loading at the blade tip. The trim state for the forward flight optimised blade leads to a reduced longitudinal cyclic angle and increased lateral cyclic, which leads to a more uniform rotor disk blade incidence distribution. The forward flight optimised blade is analysed further by extracting the rotor disk loads, shown in Figure 19. The loads are normalised by the reference chord of 1.0, equal to the chord of the first aerodynamic section.

Firstly, it must be highlighted that the loads for the baseline AH-64A are well captured during the optimisation process, as the two modes harmonic balance calculation disk loads shown in Figure 17 are similar to the loads shown in Figure 19. The greatest differences can be seen in the capturing of the negative pitching moment on the retreating side due to dynamic stall. For the forward flight optimised blade, the disk loads indicate the presence of higher-harmonic content in the lift force loading as the blade passes from the advancing side to the front of the rotor disk, which is not captured by the harmonic balance solutions (Figure 17 c)). The other features of the rotor disk loads are similar to those observed in the harmonic balance solutions. The forward flight optimised blade has a more offloaded blade tip with

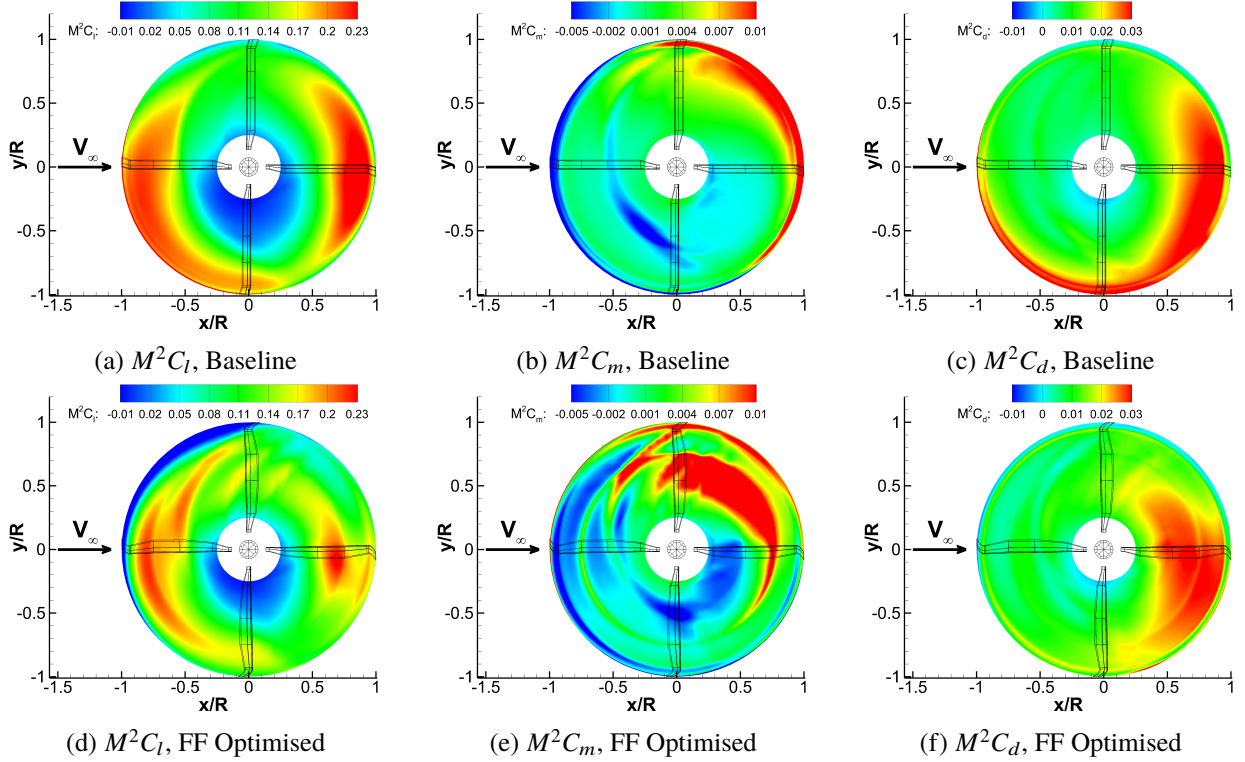


Fig. 19 Comparison of the rotor disk loads for the baseline and forward flight (FF) optimised AH-64A rotor blades in forward flight at $C_T = 0.00903$, $\mu = 0.3$ based on time-marching calculations.

increased loading inboards. A much greater pitching moment variation is seen, with a reduced in-plane force on the retreating side. The findings seen in the disk loads are analysed further by comparing the surface pressure distributions on the advancing and retreating blades, shown in Figure 20.

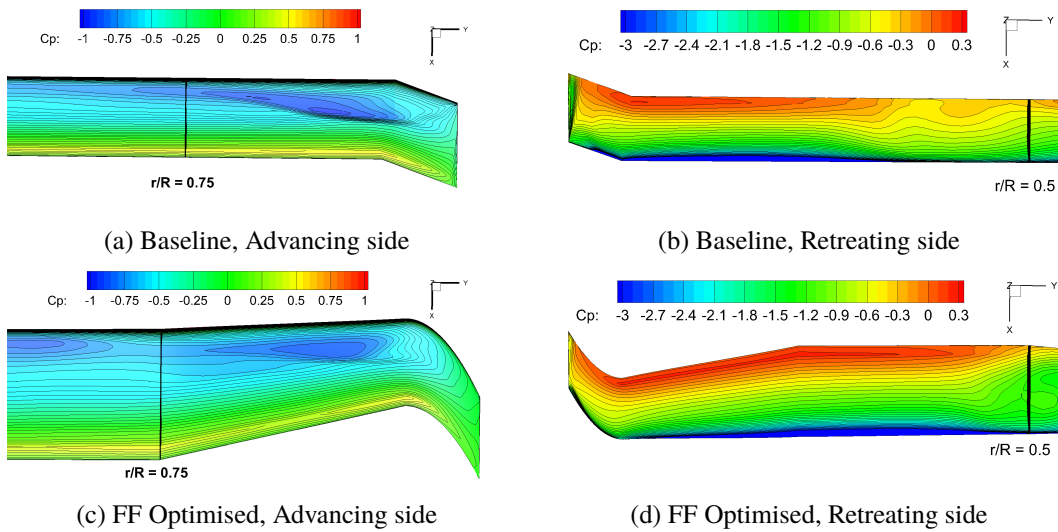


Fig. 20 Comparison between the baseline and forward flight (FF) optimised advancing and retreating side surface pressure distributions at $C_T = 0.00903$, $\mu = 0.3$.

The advancing side pressure distribution for the optimised AH-64A rotor blade indicates a much weaker advancing blade shock, leading to improved rotor performance. The shock, however, is not completely removed but moves further inboard. The optimisation setup maintained the thickness to chord ratio as the HH02 aerofoil was imposed in the region of $r/R=0.75$ to $r/R=0.943$. Therefore, the reduced chord led to stronger bunching of the pressure contours. In a future study, the chord and thickness parameters could be optimised separately to reduce the thickness to chord ratio in this region. The retreating side indicates improved pressure recovery at the trailing edge along a larger portion of the blade span. The interaction with the preceding blade tip vortex is shifted further inboard, as the optimised blade produces a weaker vortex which is affected by the mean flowfield. However, significant benefits were not expected for the retreating side aerodynamics as a low number of harmonic balance modes was used during the optimisation process, which would not accurately capture the dynamic stall event. The flow visualisation is extracted from the solution for the baseline AH-64A and forward flight optimised blades, shown in Figure 21.

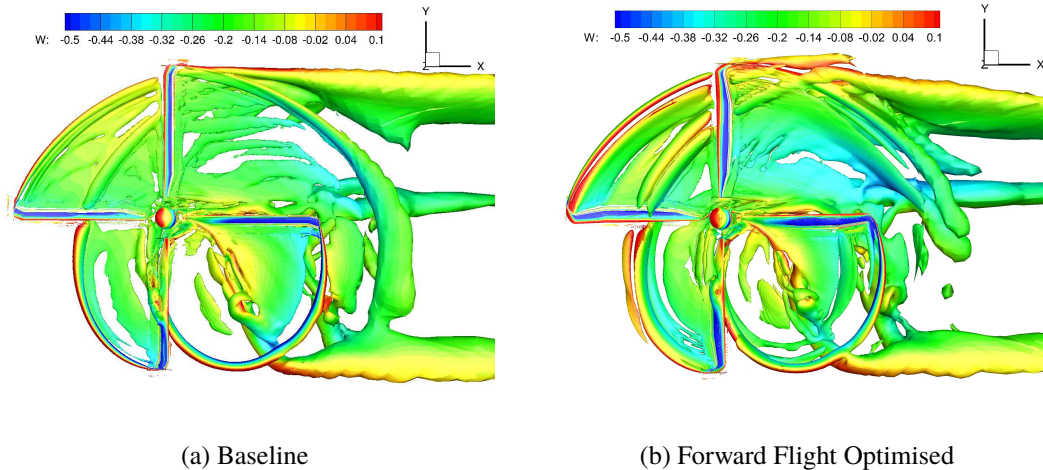


Fig. 21 Rotor wake visualization for baseline and forward flight optimised AH-64A rotor blades in forward flight at $C_T = 0.00903$, $\mu = 0.3$ using an isosurface of Q-criterion (value of 0.002) coloured by downwash velocity W .

The offloaded blade tip of the forward flight optimised blades leads to significantly weaker tip vortices which interact with the next blade leading to higher harmonic content in the rotor loads. As can be seen from Figure 21, further flow structures are shed from the blade, including multiple vortices due to the sharp dihedral-anhedral distribution. This is especially visible as the blade moves from the advancing side to the front of the rotor disk, where multiple blade vortex interactions are seen. These features could potentially lead to an increase in noise and vibration. The harmonic content of the lift force is compared for the baseline and forward flight optimised blades in Figure 22.

The 4/rev harmonic of the normal force is slightly increased for the optimised design which is the main indicated of vibration. The other lift forcing harmonics do not contribute to the fuselage vibration as they cancel each other out for a 4-bladed rotor, but can for example affect the blade root stresses. The new blade design leads to an increase in the

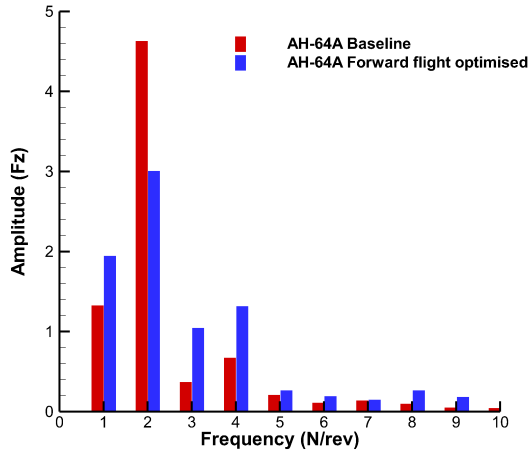


Fig. 22 Vertical force vibratory components for the baseline and forward flight AH-64A rotor blades

1/rev and 3/rev harmonic but a reduction in the 2/rev harmonic. However, no objectives or constraints were imposed on such design requirements in the present study, hence this result is not unexpected. To capture higher frequency content a high number of harmonic balance modes would have to be included within the optimisation, leading to excessive computational costs. Five modes equal to 11 snapshots could capture 3/rev, 4/rev and 5/rev components for a 4-bladed rotor in clean flight [41], with as many as 10 modes required in stalled flight due to aliasing errors from higher frequency components. The vibratory components could be optimised indirectly by an objective on the oscillatory pitching moment, or directly using the vibration index.

Based on the findings in the current rotor design study, it can be stated that the final design depends on the employed objective function. This may be one of the reasons why so many different rotor designs are seen across the globe. The forward flight optimised blade with an offloaded blade tip leads to significant performance benefits in hover and forward flight, but also leads to an increase in harmonic loading. The treatment of trim and the employed parameterisation were also proven to have an effect on the final planform shape.

Compared to the time-marching method the harmonic balance method with two modes based on a grid size of 13.1M gained a speed-up factor of 9.26. The speed-up factor was obtained based on comparing a time-marching solution of three rotor revolutions at 0.5 degrees time-steps with convergence two orders of magnitude within each time-step, and a harmonic balance simulation of 5000 iterations, showing good loads convergence and residual convergence of five orders of magnitude. This speed-up factor reduces with increasing number of harmonic balance modes. The memory requirements for the harmonic balance method showed close to $2N_H + 1$ scaling compared to the steady solution (40.9GB for steady solution, 47.1GB for the time-marching method and 205.8GB for the harmonic balance method). The adjoint-harmonic balance method with 200 Krylov Vectors used in the outer GMRES loop had a peak memory requirement of 765GB RAM, representing a factor of 3.7 compared to the baseline harmonic balance solution.

Lowering the memory requirement of the adjoint solver, whilst ensuring convergence of stiff problems is one of the key aspects considered for future work.

VI. Conclusions

This paper has demonstrated the development of a overset adjoint harmonic balance method based on the Navier-Stokes equations. The new optimisation framework has been applied to the re-design of the AH-64A rotor blade. The study showed that significant benefits are available by coupling high-fidelity CFD with optimisation methods. The main conclusions are:

- The harmonic balance method is a promising alternative compared to time-marching simulations and captures the key flow physics at reduced computational costs.
- The harmonic balance-adjoint optimisation method offers an efficient way to obtain design variable gradients for unsteady optimisation problems whilst maintaining the fidelity of the Navier-Stokes equations.
- The key drivers of an improved rotor design in hover are high blade twist and the dihedral-anhedral shape which lead to reduced blade vortex interaction and a more efficient spanwise loading distribution, by offloading the blade tip.
- In forward flight, the planform shape is more important than in hover, with a forward-backward swept planform with a reduced tip area leading to performance improvements. Similarly, as in hover, the forward flight optimised design leads to an offloaded blade tip which can also lead to increased blade harmonic loading. The imposed dihedral-anhedral distribution does not seem to be highly detrimental to the rotor power.

Future studies will include further optimisation using a weighted sum objective function approach combining hover and forward flight conditions. More elaborate objective functions should also be examined to capture the multi-disciplinary aspects of rotor design, including indicators of high noise/vibration. To capture these effects, however a higher number of harmonic balance modes would need to be used within the CFD solutions. The planform should be optimised together with the rotor control angles, whilst constraining the thrust, pitching and rolling moments. A more elaborate blade surface parameterisation should also be included to examine BERP-like designs. Finally, to further increase the fidelity of the optimisation framework, aeroelastic effects should be included.

Acknowledgements

This work is funded by DSTL (Defence Science and Technology Laboratory), Project No. 74260. A part of the technical work has been completed under the collaboration project, TTCP AER CP13.A1, Next Generation Rotor Blade Design. This work used the Cirrus UK National Tier-2 HPC Service at EPCC (<http://www.cirrus.ac.uk>). This work used the ARCHER UK National Supercomputing Service (<http://www.archer.ac.uk>).

References

- [1] Robinson, K., and Brocklehurst, A., “BERP IV Aerodynamics, Performance and Flight Envelope,” *34th European Rotorcraft Forum*, Liverpool, UK, 2008.
- [2] Rauch, P., Gervais, M., Cranga, P., Baud, A., Hirsch, J., Walter, A., and Beaumier, P., “Blue Edge (TM): The Design, Development and Testing of a New Blade Concept,” *American Helicopter Society 67th Annual Forum*, Virginia Beach, Virginia, 2011.
- [3] Boeing, “New Chinook Composite Blades Proven,” <http://www.boeing.com/features/2017/01/chinook-blades-01-17.page>, 2017. [Online; accessed 22-March-2018].
- [4] Bousman, W., and Kufeld, R., “UH-60A Airloads Catalog,” Tech. rep., National Aeronautics and Space Administration, 2005. NASA/TM-2005-212827.
- [5] Bender, G., McMullin, R., Voss, J., and Adkins, J., “First Article Preproduction Tests of the AH-64A Helicopter,” Tech. rep., US Army Aviation Systems Command, 1984. AD-A170 594.
- [6] Johnson, W., “Performance and Loads Data From a Wind Tunnel Test of a Full-Scale Rotor with Four Blade Tip Planforms,” Tech. rep., National Aeronautics and Space Administration, 1980. NASA-TM-81229.
- [7] Sandford, R., and Belko, R., “CH-47 Fiberglass Rotor Blade Design and Fabrication,” *Journal of the American Helicopter Society*, Vol. 27, No. 2, 1982. DOI: 10.4050/JAHS.27.2.43.
- [8] Perry, F., “Aerodynamics of the World Speed Record,” *43rd Annual Forum of the American Helicopter Society*, St. Louis, Missouri, 1987.
- [9] JanakiRam, R., Smith, R., Charles, B., and Hassan, A., “Aerodynamic Design of a New Affordable Main Rotor for the Apache Helicopter,” *American Helicopter Society 59th Annual Forum*, Phoenix, USA, 2003.
- [10] Johnson, W., “CAMRAD/JA: A Comprehensive Analytical Model of Rotorcraft Aerodynamics and Dynamics, Volumes 1-2,” Tech. rep., Johnson Aeronautics, Palo Alto, California, 1988.
- [11] Johnson, W., “CAMRAD II: Comprehensive Analytical Model of Rotorcraft Aerodynamics and Dynamics, Volumes I-VI,” Tech. rep., Johnson Aeronautics, Palo Alto, California, 1992-2002.
- [12] Quackenbush, T., Bliss, D., Wachspress, D., and Ong, C., “Free Wake Analysis of Hover Performance Using a New Influence Coefficient Method,” Tech. rep., National Aeronautics and Space Administration, 1990. NASA-CR-4309.
- [13] Kocurek, J., Berkowitz, L., and Harris, F., “Hover Performance Methodology at Bell Helicopter Textron,” *American Helicopter Society 36th Annual Forum*, Washington D.C., 1980.
- [14] Leusink, D., Alfano, D., Cinnella, P., and Robinet, J., “Aerodynamic rotor blade optimization at Eurocopter - a new way of industrial rotor blade design,” *51st AIAA Aerospace Sciences Meeting*, Grapevine, TX, USA, 2013.

- [15] Massaro, A., D'Andrea, A., and Benini, E., "Multiobjective-Multipoint Rotor Blade Optimization in Forward Flight Conditions Using Surrogate-Assisted Memetic Algorithms," *37th European Rotorcraft Forum*, Cascina Costa, Italy, 2011.
- [16] Desvigne, D., Coisnon, R., Michel, B., Thomas, A., Pinacho, J., and Roca-Leon, E., "Multi-Objective Industrial Optimization of High-Speed Helicopter Main Rotor Blades with Dynamically-Adpated Structural Properties," *45th European Rotorcraft Forum*, Warsaw, Poland, 2019.
- [17] ONERA, "Cooperation agreement between ONERA, JAXA and DLR for rotor optimisation research signed at Paris Air Show," <https://www.onera.fr/en/news/cooperation-agreement-between-onera-jaxa-and%20dlr-for-rotor-optimisation-research> 2019. [Online; accessed 06-April-2020].
- [18] Imiela, M., "High-fidelity optimization framework for helicopter rotors," *Journal of Aerospace Science and Technology*, Vol. 23, No. 1, 2012, pp. 2–16. DOI: 10.1016/j.ast.2011.12.011.
- [19] Le Pape, A., and Beaumier, P., "Numerical Optimization of Helicopter Rotor Aerodynamic Performance in Hover," *29th European Rotorcraft Forum*, Friedrichshafen, Germany, 2003.
- [20] Dumont, A., Le Pape, A., Peter, J., and Huberson, S., "Aerodynamic Shape Optimization of Hovering Rotors Using a Discrete Adjoint of the Reynolds-Averaged Navier-Stokes Equations," *Journal of the American Helicopter Society*, Vol. 56, No. 3, 2011, pp. 1–11. DOI: 10.4050/JAHS.56.032002.
- [21] Lyu, Z., Xu, Z., and Martins, J., "Benchmarking Optimization Algorithms for Wing Aerodynamic Design Optimization," *The Eighth International Conference on Computational Fluid Dynamics(ICCFD8)*, Chengdu, Sichuan, China, 2004.
- [22] Sugiura, M., Tanabe, Y., Aoyama, T., Ortun, B., and Bailly, J., "An ONERA/JAXA Co-operative Research on the Assessment of Aerodynamic Methods for the Optimization of Helicopter Rotor Blades, Phase II," *42nd European Rotorcraft Forum*, Lille, France, 2016.
- [23] Johnson, C., and Barakos, G., "Optimizing Rotor Blades with Approximate British Experimental Rotor Programme Tips," *Journal of Aircraft*, Vol. 51, No. 2, 2014, pp. 447–463. DOI: 10.2514/1.C032042.
- [24] Zhu, Z., and Zhao, Q., "Optimization for rotor blade-tip planform with low high-speed impulsive noise characteristics in forward flight," *Proc IMechE Part G: Journal of Aerospace Engineering*, Vol. 231, No. 7, 2017, pp. 1312–1324. DOI: 10.1177/0954410016650908.
- [25] Zhao, Q., Zhu, Z., Yuan, X., and Wang, B., "Aerodynamic Geometry Optimization of Coaxial Rigid Rotors in Forward Flight," *American Helicopter Society 74th Annual Forum*, Phoenix, AZ, USA, 2018.
- [26] Bailly, J., and Bailly, D., "Multifidelity Aerodynamic Optimization of a Helicopter Rotor Blade," *AIAA Journal*, Vol. 57, No. 8, 2019, pp. 3132–3144. DOI: 10.2514/1.J056513.
- [27] Wilke, G., "Multi-Objective Optimizations in Rotor Aerodynamics using Variable Fidelity Simulations," *39th European Rotorcraft Forum*, Moscow, Russia, 2013.

- [28] Kenway, G., and Martins, J., “High-fidelity aerostructural optimization considering buffet onset,” *AIAA Aviation 16th AIAA/ISSMO Multidisciplinary Analysis and Optimization Conference*, Dallas, TX, USA, 2015.
- [29] Nielsen, E., and Diskin, B., “Discrete Adjoint-Based Design for Unsteady Turbulent Flows On Dynamic Overset Unstructured Grids,” *AIAA Journal*, Vol. 51, No. 6, 2013, pp. 1355–1373. DOI: 10.2514/1.J051859.
- [30] Wang, L., Diskin, B., Biedron, R., Nielsen, E., and Bachau, O., “High-Fidelity Multidisciplinary Sensitivity Analysis and Design Optimization for Rotorcraft Applications,” *AIAA Journal*, Vol. 57, No. 8, 2019, pp. 1–15. DOI: 10.2514/1.J056587.
- [31] Mishra, A., Mani, K., Mavriplis, D., and Sitaraman, J., “Helicopter Rotor Design using Adjoint-based Optimization in a Coupled CFD-CSD Framework,” *American Helicopter Society 69th Annual Forum*, Phoenix, AZ, USA, 2013.
- [32] Fabiano, E., and Mavriplis, D., “Adjoint-based Aeroacoustic Design-Optimization of Flexible Rotors in Forward Flight,” *American Helicopter Society 72nd Annual Forum*, West Palm Beach, FL, USA, 2016.
- [33] Wang, Q., Moin, P., and Iaccarino, G., “Minimal repetition dynamic checkpointing algorithm for unsteady adjoint calculation,” *SIAM Journal on Scientific Computing*, Vol. 31, No. 4, 2009, pp. 2549–2567. DOI: 10.1137/080727890.
- [34] Beran, P., Stanford, B., and Kurdi, M., “Sensitivity Analysis for Optimization of Dynamic Systems with Reduced Order Modeling,” *48th AIAA Aerospace Sciences Meeting*, Orlando, FL, USA, 2010.
- [35] Hall, K., Thomas, J., and Clark, W., “Computation of Unsteady Nonlinear Flows in Cascades Using a Harmonic Balance Technique,” *AIAA Journal*, Vol. 40, No. 5, 2002, pp. 879–886. DOI: 10.2514/2.1754.
- [36] Sicot, F., Gomar, A., Dufour, H., and Dugeai, A., “Time-Domain Harmonic Balance Method for Turbomachinery Aeroelasticity,” *AIAA Journal*, Vol. 52, No. 1, 2014, pp. 62–71. DOI: 10.2514/1.J051848.
- [37] van der Weide, E., Gopinath, A., and Jameson, A., “Turbomachinery Applications with the Time Spectral Method,” *35th AIAA Fluid Dynamics Conference and Exhibit*, Toronto, Ontario, 2005.
- [38] Ekici, K., Hall, K., and Dowell, E., “Computationally fast harmonic balance methods for unsteady aerodynamic predictions of helicopter rotors,” *Journal of Computational Physics*, Vol. 227, No. 12, 2008, pp. 6206–6225. DOI: 10.1016/j.jcp.2008.02.028.
- [39] Butsuntorn, N., and Jameson, A., “Time Spectral Method for Rotorcraft Flow,” *46th AIAA Aerospace Sciences Meeting and Exhibit*, Reno, Nevada, 2008.
- [40] Choi, S., Alonso, J., van der Weide, E., and Sitaraman, J., “Validation Study of Aerodynamic Analysis Tools for Design Optimization of Helicopter Rotors,” *25th AIAA Applied Aerodynamics Conference*, Miami, Florida, 2007.
- [41] Choi, S., and Datta, A., “Time-Spectral Method for CFD Prediction of Helicopter Rotor Vibratory Loads,” *5th International Conference on CFD*, Seoul, Republic of Korea, 2008.
- [42] Woodgate, M., and Barakos, G., “Implicit Computational Fluid Dynamics Methods for Fast Analysis of Rotor Flows,” *AIAA Journal*, Vol. 50, No. 6, 2012, pp. 1217–1244. DOI: 10.2514/1.J051155.

- [43] Li, H., and Ekici, K., “Aeroelastic Modeling of the AGARD 445.6 Wing Using the Harmonic-Balance-Based One-shot Method,” *AIAA Journal*, Vol. 57, No. 11, 2019, pp. 4885–4902. DOI: 10.2514/1.J058363.
- [44] Nadarajah, S., “Convergence studies of the time accurate and non-linear frequency domain methods for optimum shape design,” *International Journal of Computational Fluid Dynamics*, Vol. 21, No. 5-6, 2007, pp. 189–207. DOI: 10.1080/10618560701577328.
- [45] Huang, H., and Ekici, K., “A discrete adjoint harmonic balance method for turbomachinery shape optimization,” *Journal of Aerospace Science and Technology*, Vol. 39, 2014, pp. 481–490. DOI: 10.1016/j.ast.2014.05.015.
- [46] Rubino, A., Pini, M., Colonna, P., Albring, T., Nimmagadda, S., Economou, T., and Alonso, J., “Adjoint-based fluid dynamic design optimization in quasi-periodic unsteady flow problems using a harmonic balance method,” *Journal of Computational Physics*, Vol. 372, 2018, pp. 220–235. DOI: 10.1016/j.jcp.2018.06.023.
- [47] Rubino, A., “Reduced Order Models For Unsteady Fluid Dynamic Optimization of Turbomachinery,” Ph.D. thesis, University of Delft, 2019.
- [48] Vitale, S., Pini, M., and Colonna, P., “Multistage Turbomachinery Design Using the Discrete Adjoint Method Within the Open-Source Software SU2,” *Journal of Propulsion and Power*, Vol. 36, No. 3, 2020, pp. 465–478. DOI: 10.2514/1.B37685.
- [49] He, S., Jonsson, E., Mader, C., and Martins, J., “Aerodynamic Shape Optimization with Time Spectral Flutter Adjoint,” *AIAA SciTech Forum*, San Diego, California, 2019.
- [50] Prasad, R., and Choi, S., “Aerodynamic Shape Optimization for Flutter/LCO based design using Coupled Adjoint,” *AIAA SciTech Forum*, Orlando, FL, 2020.
- [51] He, S., Luder, A., Mader, C., Maki, K., and Martins, J., “A Time-Spectral Adjoint Approach for Aerodynamic Shape Optimization Under Periodic Wakes,” *AIAA SciTech Forum*, Orlando, FL, 2020.
- [52] Choi, S., Lee, K., Potsdam, M., and Alonso, J., “Helicopter Rotor Design Using a Time-Spectral and Adjoint-Based Method,” *Journal of Aircraft*, Vol. 51, No. 2, 2014, pp. 412–423. DOI: 10.2514/1.C031975.
- [53] Kim, H., “Coupled Adjoint-based Sensitivity Analysis using a FSI Method in Time Spectral Form,” Ph.D. thesis, Virginia Polytechnic Institute and State University, 2019.
- [54] Steijl, R., Barakos, G. N., and Badcock, K., “A framework for CFD analysis of helicopter rotors in hover and forward flight,” *International Journal for Numerical Methods in Fluids*, Vol. 51, No. 8, 2006, pp. 819–847. DOI: 10.1002/d.1086.
- [55] Steijl, R., and Barakos, G. N., “Sliding mesh algorithm for CFD analysis of helicopter rotor-fuselage aerodynamics,” *International Journal for Numerical Methods in Fluids*, Vol. 58, No. 5, 2008, pp. 527–549. DOI: 10.1002/d.1757.
- [56] Osher, S., and Chakravarthy, S., “Upwind schemes and boundary conditions with applications to Euler equations in general geometries,” *Journal of Computational Physics*, Vol. 50, No. 3, 1983, pp. 447–481. DOI: 10.1016/0021-9991(83)90106-7.

- [57] van Leer, B., “Towards the ultimate conservative difference scheme. V.A second-order sequel to Godunov’s Method,” *Journal of Computational Physics*, Vol. 32, No. 1, 1979, pp. 101–136. DOI: 10.1016/0021-9991(79)90145-1.
- [58] van Albada, G. D., van Leer, B., and Roberts, W. W., “A Comparative Study of Computational Methods in Cosmic Gas Dynamics,” *Astronomy and Astrophysics*, Vol. 108, No. 1, 1982, pp. 76–84. DOI: 10.1007/978-3-642-60543-7.
- [59] Jameson, A., “Time-Dependent Calculations Using Multigrid, with Applications to Unsteady Flows past Airfoils and Wings,” *AIAA 10th Computational Fluid Dynamics Conference*, Honolulu, HI, USA, 1991.
- [60] Axelsson, O., *Iterative Solution Methods*, Cambridge University Press: Cambridge, MA, 1994.
- [61] Woodgate, M., and Barakos, G., “An Implicit Hybrid Method for the Computation of Rotorcraft Aerodynamic Flows,” *AIAA SciTech Forum, 54th Aerospace Sciences Meeting*, 2016.
- [62] Menter, F. R., “Two-Equation Eddy-Viscosity Turbulence Models for Engineering Applications,” *AIAA Journal*, Vol. 32, No. 8, 1994, pp. 1598–1605. DOI: 10.2514/3.12149.
- [63] Fitzgibbon, T., Woodgate, M., and Barakos, G., “Assessment of the Harmonic Balance Method for Rotor Blade Performance Predictions,” *45th European Rotorcraft Forum*, Warsaw, Poland, 2019.
- [64] Saad, Y., and Schultz, M., “GMRES: A Generalized Minimal Residual Algorithm for Solving Nonsymmetric Linear Systems,” *SIAM Journal on Scientific and Statistical Computing*, Vol. 7, No. 3, 1986, pp. 856–869. DOI: 10.1137/0907058.
- [65] Hascoët, L., and Pascual, V., “The Tapenade Automatic Differentiation tool: Principles, Model, and Specification,” *ACM Transactions On Mathematical Software*, Vol. 39, No. 3, 2013. URL <http://dx.doi.org/10.1145/2450153.2450158>.
- [66] Biava, M., Woodgate, M., and Barakos, G., “Fully Implicit Discrete-Adjoint Methods for Rotorcraft Applications,” *AIAA Journal*, Vol. 54, No. 2, 2016, pp. 735–748. DOI: 10.2514/1.J054006.
- [67] Biava, M., and Barakos, G., “Optimisation of Ducted Propellers for Hybrid Air Vehicles Using High-Fidelity CFD,” *Aeronautical Journal*, Vol. 120, No. 1232, 2016, pp. 1632–1657. DOI: 10.1017/aer.2016.78.
- [68] Kraft, D., “Algorithm 733: TOMP-Fortran Modules for Optimal Control Calculations,” *ACM Transactions on Mathematical Software*, Vol. 20, No. 3, 1994, pp. 262–281. DOI: 10.1145/192115.192124.
- [69] Liu, C., and Nocedal, J., “On the limited memory BFGS method for large scale optimization,” *Math. Programming*, Vol. 45, 1989, pp. 503–528. DOI: 10.1007/BF01589116.
- [70] Bernstein, S., “Demonstration du theoreme de Weierstrass fondee sur le calcul desprobabilites,” *Comm. Kharkov Math. Soc.*, Vol. 13, 1912, pp. 1–2.
- [71] Bender, G., Diekmann, V., Ottomeyer, J., Picasso III, B., and Higgins, L., “Engineering Design Test 4, YAH-64 Advanced Attack Helicopter ,” Tech. rep., United States Army Engineering Flight Activity, 1980. USAAEFA NO. 80-03.

- [72] Berry, J., "Helicopter Blade Dynamic Loads Measured During Performance Testing of Two Scaled Rotors," Tech. rep., National Aeronautics and Space Administration, 1987. NASA-TM-89053.
- [73] WJ. McCroskey and KW. McAlister and LW. Carr and SL. Pucci, "An Experimental Study of Dynamic Stall on Advanced Airfoil Sections Volume 1. Summary of the Experiment," Tech. rep., National Aeronautics and Space Administration, 1982. NASA-TM-84245.
- [74] Loftin Jr., L., "Theoretical and Experimental Data for a number of NACA 6A-Series airfoil sections," Tech. rep., National Aeronautics and Space Administration, 1948. NASA-TR-903.
- [75] Srinivasan, G., Raghavan, V., and Duque, E., "Flowfield Analysis of Modern Helicopter Rotors in Hover by Navier-Stokes Method," *International Technical Specialists Meeting on Rotorcraft Acoustics and Rotor Fluid Dynamics*, Philadelphia, PA, USA, 1991.
- [76] Kunz, D., and Jones, H., "Modelling and Simulation of the Apache Rotor System in CAMRAD II," *American Helicopter Society Structure Specialists' Meeting*, Williamsburg, VA, USA, 2001.